frontiers in Physics

REVIEW
published: 16 July 2021
doi: 10.3389/fphy.2021.675134

Quantum Control of Coherent π-Electron Dynamics in Aromatic Ring Molecules

Hirobumi Mineo[1,2]*, *Ngoc-Loan Phan*[3] *and Yuichi Fujimura*[4]*

[1]Atomic Molecular and Optical Physics Research Group, Advanced Institute of Materials Science, Ton Duc Thang University, Ho Chi Minh City, Vietnam, [2]Faculty of Applied Sciences, Ton Duc Thang University, Ho Chi Minh City, Vietnam, [3]Department of Physics, Ho Chi Minh City University of Education, Ho Chi Minh City, Vietnam, [4]Department of Chemistry, Graduate School of Science, Tohoku University, Sendai, Japan

Herein we review a theoretical study of unidirectional π-electron rotation in aromatic ring molecules, which originates from two quasi-degenerate electronic excited states created coherently by a linearly polarized ultraviolet/visible laser with a properly designed photon polarization direction. Analytical expressions for coherent π-electron angular momentum, ring current and ring current-induced magnetic field are derived in the quantum chemical molecular orbital (MO) theory. The time evolution of the angular momentum and the ring current are expressed using the density matrix method under Markov approximation or by solving the time-dependent Schrödinger equation. In this review we present the results of the following quantum control scenarios after a fundamental theoretical description of coherent angular momentum, ring current and magnetic field: first, two-dimensional coherent π-electron dynamics in a non-planar (*P*)-2,2'-biphenol molecule; second, localization of the coherent π-electron ring current to a designated benzene ring in polycyclic aromatic hydrocarbons; third, unidirectional π-electron rotations in low-symmetry aromatic ring molecules based on the dynamic Stark shift of two relevant excited states that form a degenerate state using the non-resonant ultraviolet lasers. The magnetic fields induced by the coherent π-electron ring currents are also estimated, and the position dependence of the magnetic fluxes is demonstrated.

Keywords: quantum control, electron dynamics, coherent ring current, ring current localization, angular momentum, quantum switching, Stark-induced degenerate electronic state

OPEN ACCESS

Edited by:
Philip Bucksbaum,
Stanford University, United States

Reviewed by:
Sheng Meng,
Institute of Physics (CAS), China
Luca Evangelisti,
University of Bologna, Italy

***Correspondence:**
Hirobumi Mineo
mineo@tdtu.edu.vn
Yuichi Fujimura
fujimurayuichi@m.tohoku.ac.jp

Specialty section:
This article was submitted to Physical Chemistry and Chemical Physics, a section of the journal Frontiers in Physics

Received: *02 March 2021*
Accepted: *23 June 2021*
Published: *16 July 2021*

Citation:
Mineo H, Phan N-L and Fujimura Y (2021) Quantum Control of Coherent π-Electron Dynamics in Aromatic Ring Molecules. Front. Phys. 9:675134. doi: 10.3389/fphy.2021.675134

1 INTRODUCTION

Recent progress in laser science and technology has facilitated the coherent control of ultrafast charge migration dynamics in molecular systems [1–21]. Controlled charge migration can generate unidirectional currents and current-induced magnetic fields, which can be used as a guiding principle for the next-generation ultrafast optoelectronic devices [22, 23]. Laser control of π-electron rotations in aromatic ring molecules is a typical example. Pioneering studies on the generation of coherent π-electron rotations in high-symmetry ring molecules such as Mg porphyrin having degenerate excited states have been reported by the Manz group [24–26]. π-Electron rotations were induced by degenerate electronic excited states, which were coherently created by circularly polarized ultraviolet (UV) lasers. The generation mechanism of the photon angular momentum involves the photon transfer from the circularly polarized UV lasers to the π-electrons, thereby the left- or right-handed circular

polarization of the applied laser defines the rotational direction of the angular momentum [27]. In contrast in ring molecules with low-symmetry π-electrons cannot be rotated by using the circularly polarized lasers, due to the absence of electronic excited states degenerate, that would receive the photon angular momentum. Thus, it was commonly understood that coherent π-electron rotations could not be generated in low-symmetry aromatic ring molecules. However, Kanno et al. [28–31] have invalidated this long-established understanding by demonstrating that π-electrons in oriented chiral aromatic ring molecules can be rotated by the coherent excitation of a pair of quasi-degenerate π-electronic excited states using a linearly polarized UV/vis laser pulse with a properly designed photon polarization direction [28, 29]; the polarization direction of the pulse determines the initial direction of the π-electron rotation, whether right- or left-handed one. The duration of the unidirectional rotation is inversely proportional to the energy difference between the two quasi-degenerate excited states, and inverse rotation begins after the duration because the coherent state is not a nonstationary state rather than an eigenstate. Pump and dump laser pulses with their properly designed polarization directions for these lasers are applied to eliminate the reverse rotation. The number of unidirectional rotations during the duration can be estimated from the energy difference between the quasi-degenerate excited and ground states. This only applies to the ideal case in which any dephasing processes disturbing the electronic coherence are omitted. It is expected that unidirectional ring currents produce much stronger magnetic fields than traditional static magnetic fields [32, 33].

The concept of the conventional ring current has already been established previously and plays an important role in interpreting the magnetic properties and aromaticity of conjugated molecular systems [34, 35]. The molecules investigated based on the ring current are in the ground state, and the current densities for evaluation of the ring current are calculated using the first-order electronic wave function in the time-independent magnetic field and in a permanent magnetic dipole. Such a conventional ring current should be called an incoherent current.

In this article, we present the most recent results of our theoretical studies on the quantum control of coherent π→electron rotations in low-symmetry aromatic ring molecules. Low-symmetry aromatic ring molecules are not rare, but rather common: high-symmetry aromatic molecules often become low-symmetry ones by substitution of a functional group, or under environment conditions. In the next section, the fundamental theory for the quantitative analysis of coherent π-electrons in a low-symmetry aromatic ring molecule is introduced. Here, the time-dependent coherent angular momentum, ring current, and ring current-induced magnetic field are analytically derived in a closed form in the quantum chemical MO theory. Time-evolutions of these quantities are derived by the density matrix method [36–39]. The temporal behavior of coherence is determined by the off-diagonal element of density matrix. Then, the Markov approximation is ultilized for considering the dephasing effects on the conherent angular momenta and ring currents. The magnitudes of the electronic angular momenta and ring currents are expressed as the summation of the expectation values of the corresponding one-electron operators in the aromatic rings. The bond current between the nearest neighbor carbon atoms, C_i and C_j, is defined as an electric current flowing through a half plane perpendicular to the $C_i - C_j$ bond. The coherent bond current in an aromatic ring is defined as the average of all bond currents. The application of this theory to a nonplanar chiral aromatic molecule, (*P*)-2,2'-biphenol, is briefly described. (*P*)-2,2'-biphenol has four patterns of coherent π-electron rotations along with the two phenol rings because of its nonplanar geometrical structure [39, 40]. A sequence of the four rotational patterns can be controlled through a coherent excitation of two electronic states with two requirements: the symmetry of the two electronic states, and their relative phase. Quantum switching of coherent π-electron rotations is proposed [40]. In **Section 3**, the key points are summarized for the application of the quantum optimal control method for controlling coherent ring currents in polycyclic aromatic hydrocarbons (PAHs). These molecules exhibit several localization patterns of coherent π-electron rotations. Therefore, how to set up the target state for a desired localization pattern is crucial [41, 42]. However, we demonstrate that the target state can easily be set up using the Lagrange multiplier method. As examples, two types of current localizations for the simplest PAH, anthracene, are adopted [42]: current localization to the designated benzene ring, and the perimeter ring current. In **Section 4**, a convenient scenario involving unidirectional π-electron rotations in low-symmetry aromatic ring molecules is described [43]. The basic idea behind unidirectional electron rotations is to degenerate two nondegenerate excited states by utilizing dynamic Stark shifts. A degenerate state induced by dynamic Stark shifts is called a dynamic Stark-induced degenerate electronic state (DSIDES). Two linearly polarized continuous lasers with different frequencies and phases are used to form a DSIDES, where each laser is set to selectively interact with each electronic state through non-resonant excitation. As a result, the unidirectional π-electron rotation is driven by the lasers. This scenario was applied to toluene. The resulting angular momenta can be represented by a pulse train having an angular momentum. Each angular momentum pulse represents the unidirectional π-electrons rotation, which begins with acceleration and ends with deceleration.

2 COHERENT π-ELECTRON DYNAMICS IN LOW-SYMMETRY AROMATIC RING MOLECULES

In this section we present the theoretical formalism for the coherent π-electrons in a low-symmetry aromatic ring molecule to derive analytical expressions for the coherent angular momentum, ring current and the current-induced magnetic field within the framework of the quantum chemical MO treatment [39, 40].

2.1 Equations of Motion for Coherent π-Electron Rotations Induced by Ultrashort UV/Vis Lasers

The expectation values of the coherent π−electron angular momentum and the ring current operators in an aromatic molecule are generally expressed as

$$\langle \widehat{O}(t) \rangle = n \int d^3\mathbf{r}_1 \cdots d^3\mathbf{r}_n \Psi^*(t) \widehat{O}(r) \Psi(t). \tag{1}$$

Here, $\widehat{O}(r)$ is a single-electron operator for the angular momentum or current. $\Psi(t)$ is the wave function of the π−electrons in laser field $\mathbf{F}(t)$ at time t, n denotes the number of electrons, and $\mathbf{r}_i$ express the ith electron coordinates. Since the optically-allowed electronic excited states of the conjugated aromatic rings are of our interest, the electronic wave function can be expanded by the two electronic configurations, i.e., the ground configuration $\mathbf{\Phi}_0$, and the singly excited ones $\mathbf{\Phi}_\alpha$ as

$$\Psi(t) = c_0(t)\mathbf{\Phi}_0 + \sum_\alpha c_\alpha(t)\mathbf{\Phi}_\alpha, \tag{2}$$

where $\mathbf{\Phi}_0$ is defined by a single Slater determinant as $\Phi_0(\mathbf{r}_1, \cdots, \mathbf{r}_n) = \|\phi_1 \cdots \phi_a \cdots \phi_b \cdots \phi_n\|$ with $\phi_n \equiv \phi_n(\mathbf{r}_n)$. Here, ϕ_a and ϕ_b are the occupied orbitals, Φ_α is the electronic wave function for a single electron excited configuration $\alpha : a \rightarrow a'$, i.e., the single electron transition from the occupied molecular orbital (MO) a to the unoccupied MO a', when $\Phi_\alpha(\mathbf{r}_1, \cdots, \mathbf{r}_n) = \|\phi_1 \cdots \phi_{a'} \cdots \phi_b \cdots \phi_n\|$.

The coherent and incoherent temporal behaviors of the electrons induced by a laser field $\mathbf{F}(t)$ can be obtained directly by solving the coupled electronic equations of motion expressed by the density matrix elements $\rho_{\alpha\beta}(t)$ under the initial population conditions $\rho_{00}(0) = 1$ and $\rho_{\alpha\alpha}(0) = 0$ for $\alpha \neq 0$ and $\rho_{\alpha\beta}(0) = 0$ for $\alpha \neq \beta$, that is, there is no electronic coherence at the initial time such that

$$\frac{d\rho_{\alpha\beta}(t)}{dt} = -\frac{i}{\hbar}\sum_\gamma \Big(V_{\alpha\gamma}(t)\rho_{\gamma\beta}(t) - \rho_{\alpha\gamma}(t)V_{\gamma\beta}(t) \Big) - \big(i\omega_{\alpha\beta} + \gamma_{\alpha\beta} \big)\rho_{\alpha\beta}(t). \tag{3}$$

Here, $\rho_{\alpha\beta}(t) \equiv c_\alpha(t)c_\beta^*(t)$ is the density matrix element, and $V_{\alpha\gamma}(t)$ is the coupling matrix element between states α and γ *via* the molecule-laser interaction $\widehat{V}(t) = -\boldsymbol{\mu} \cdot \mathbf{F}(t)$, where $\boldsymbol{\mu}$ denotes the transition dipole moment operator, $\gamma_{\alpha\beta}\big(= \frac{1}{2}(\gamma_\alpha + \gamma_\beta) + \gamma^{(d)}_{\alpha\gamma} \big)$ are the dephasing constants in the Markov approximation [38, 39] and $\omega_{\beta\alpha}$is the frequency difference between the two electronic states α and β. Here, $\gamma_\alpha(\gamma_\beta)$ is the non-radiative transition rate constant of the electronic state $\alpha(\beta)$, and $\gamma^{(d)}_{\alpha\beta}$ are the pure dephasing constants induced by the elastic interaction between the heat bath and molecule of interest.

Because we are interested in the coherent behaviors of dipole-allowed quasi-degenerate π-electronic excited states in the visible or UV region of an aromatic ring molecule, **Eq. 1** can be rewritten in terms of singly excited configurations $\{\Phi_\kappa\}$ if $\kappa \neq 0$ as

$$\langle O(t) \rangle = n \int d^3\mathbf{r}_1 \cdots d^3\mathbf{r}_n \mathrm{Tr}\big(\rho(t)O(r)\big), \tag{4}$$

where $O_{\alpha\beta}(r) = \langle \Phi_\alpha | \widehat{O}(r) | \Phi_\beta \rangle$.

In **Eq. 4**, the coherence between singly excited state configurations is considered, and the coherence between the ground state and the excited state is neglected because this coherence is much shorter compared to that between the singly excited state configurations. In this case, the coherence time is proportional to the inverse of the energy gap between the two electronic states.

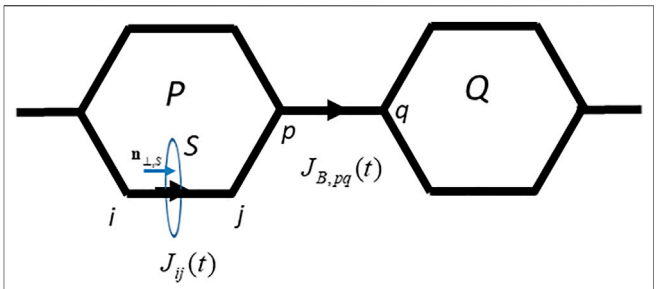

FIGURE 1 | The interatomic bond current $J_{ij}(t)$ and bridge bond current $J_{B,pq}(t)$ are depicted. Here, i and j indicate the positions of two atomic sites in the bond C_i – C_j, and each carbon atom C_p, or C_q belongs to a different aromatic ring P or Q, which are in neighbors.

The coherent π-electron angular momentum is formulated in the quantum chemical MO theory, and the π-orbital ϕ_k associated with the optical transition is expanded in terms of a linear combination of atomic orbitals χ_i as

$$\phi_k = \sum_i c_{k,i}\chi_i, \ (k = a, a', b, b'), \tag{5}$$

where χ_i denotes the atomic orbital, and $c_{k,i}$ indicates the molecular orbital coefficient.

Equation 4 can be expressed by using the **Eq. 5** as

$$\langle \widehat{O}(t) \rangle = 2n \sum_{\alpha<\beta} \mathrm{Im}\ \rho_{\beta\alpha}(t) \sum_{ij} \Big(\delta_{ab}c^*_{a'i}c_{b'j} + \delta_{a'b'}c^*_{ai}c_{bj} \Big) \int d^3r \chi_i^* i\widehat{O}(r)\chi_j. \tag{6}$$

Here, the temporal behavior of the expectation value $\langle \widehat{O}(t) \rangle$ can be expressed using the off-diagonal density matrix element $\rho_{\beta\alpha}(t)$. The suffixes (a, a') $((b, b'))$ corresponds to the electronic configurations $\alpha(\beta)$, respectively.

2.2 Coherent π-Electron Angular Momentum

Consider the spatially fixed aromatic ring molecule with N aromatic rings. The electron angular momentum operator is defined as $\widehat{O}(\mathbf{r}) = \mathbf{l}_Z = \sum_K \widehat{O}_K(\mathbf{r})$ with $\widehat{O}_K(\mathbf{r}) = \mathbf{l}_{Z,K} = -i\hbar(x_K\partial/\partial y_K - y_K\partial/\partial x_K)\mathbf{n}_{\perp,K}$. Here $\mathbf{l}_{Z,K}$is the electronic angular momentum operator of the component perpendicular to ring K. Coordinates x_K and y_K are defined on the aromatic ring K, and $\mathbf{n}_{\perp,K}$ is the unit vector perpendicular to the aromatic ring. The expectation value of Kth angular momentum operator is given in terms of a $2p_z$ carbon atomic orbitals (AOs) as

$$\begin{aligned} \mathbf{l}_{Z,K}(t) \equiv & \int d^3r_K \langle \Psi(t) | \mathbf{l}_{Z,K} | \Psi(t) \rangle \\ = & -2n_e\hbar\,\mathbf{n}_{\perp,K} \sum_{\alpha<\beta} \mathrm{Im}\,\rho_{\beta\alpha}(t) \sum_{ij\in K} \Big(\delta_{ab}c^*_{a'i}c_{b'j} + \delta_{a'b'}c^*_{ai}c_{bj} \Big) \\ & \times \int d^3r \chi_i^* \left(x\frac{\partial}{\partial y} - y\frac{\partial}{\partial x} \right) \chi_j, \end{aligned} \tag{7}$$

where n_e is the total number of electrons in the system.

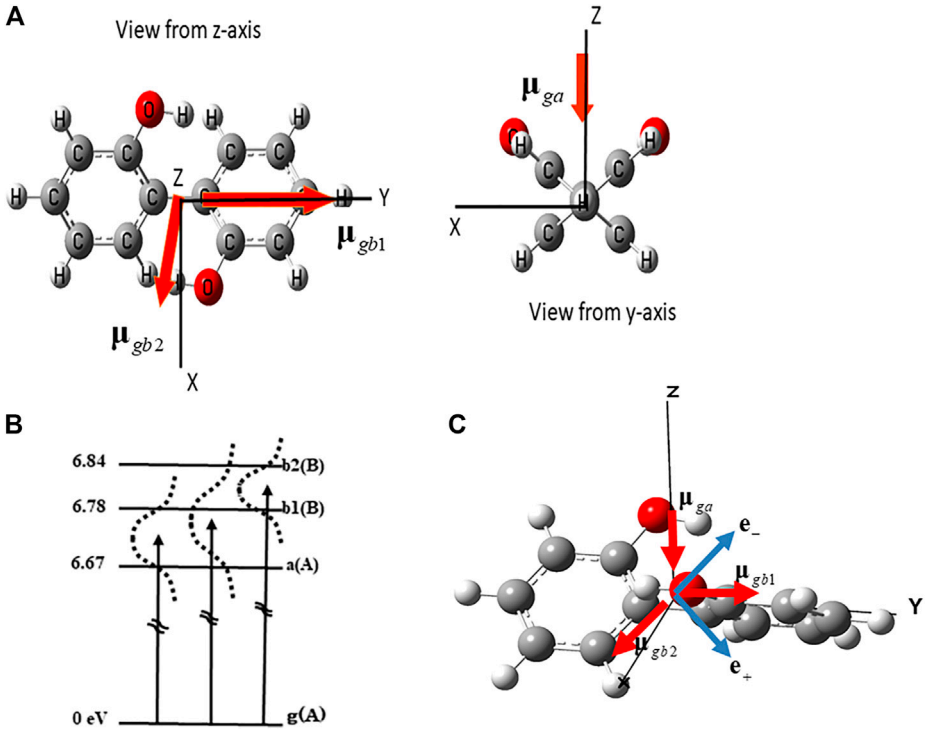

FIGURE 2 | (A) Geometrical structure of (*P*)-2,2'-biphenol belonging to point group C_2 and the transition dipole moments between the ground state (g) and three excited states *a*, b_1 and b_2. **(B)** Three electronic excited states and the dipole allowed transitions used to create the coherent electronic states. A and B are the irreducible representations of point group C_2. Dotted lines indicate the laser band widths that cover the superpositions of two electronic excited states (a b_1), (a b_2) and (b_1 b_2) respectively. **(C)** Linearly polarized unit vector of laser $\mathbf{e}_+$ ($\mathbf{e}_-$) used to generate the in-phase superposition (a+b_1) (out-of-phase superposition (a-b_1)).

Note that in **Eq. 7** the dependence of the electron angular momentum on the laser intensity is reflected in the imaginary part of the off-diagonal density matrices Im $\rho_{\beta\alpha}(t)$.

2.3 Coherent π-Electron Ring Current

From **Eq. 6**, the perpendicular component of the time-dependent electric current flowing through a surface *S* (*See* **Figure 1**) is generally defined as

$$\langle J(t)\rangle = 2n_e \sum_{\alpha<\beta} \mathrm{Im}\,\rho_{\beta\alpha}(t) \sum_{ij} \left(\delta_{ab} c^*_{a'i} c_{b'j} + \delta_{a'b'} c^*_{ai} c_{bj}\right) \int d^3r \chi^*_i i\hat{J}(\mathbf{r}) \chi_j. \tag{8}$$

Here $\hat{J}(\mathbf{r}) = \frac{e\hbar}{2m_e i}\left(\overrightarrow{\nabla} - \overleftarrow{\nabla}\right)$ is the current density operator. $\overrightarrow{\nabla}$ ($\overleftarrow{\nabla}$) is the nabla operating on the atomic orbital on the right-hand side (left-hand side).

Equation 8 can be expressed as

$$\langle J(t)\rangle = \sum_{i<j} J_{ij}(t), \tag{9}$$

where

$$J_{ij}(t) = 2n_e \sum_{\alpha<\beta} \mathrm{Im}\,\rho_{\beta\alpha}(t) \left(\delta_{ab}\left(c^*_{a'i} c_{b'j} - c^*_{b'i} c_{a'j}\right) + \delta_{a'b'}\left(c^*_{ai} c_{bj} - c^*_{bi} c_{aj}\right)\right) J_{ij}, \tag{10a}$$

with

$$J_{ij} = \int_S d^2 r_\perp \chi^*_i \mathbf{n}_{\perp,S} \cdot \overrightarrow{\nabla} \chi_j, \tag{10b}$$

where $\mathbf{n}_{\perp,S}$ is a unit vector perpendicular to a surface *S*, which is given as $\mathbf{n}_{\perp,S} = \frac{\mathbf{r}_j - \mathbf{r}_i}{|\mathbf{r}_j - \mathbf{r}_i|}$, and the surface *S* is set at the center of the carbon bond $C_i - C_j$. The surface integrations in **Eqs. 8**, **10b** are carried out over the half-plane *S* (*see* **Figure 1**). Using Slater type AOs for $\{\chi_i\}$, J_{ij} in **Eq. 10b** can be expressed in analytical form [40].

We introduce the *bridge bond current* $J_{B,pq}(t)$ which is a specific case of an interatomic bond current, and is defined as the current bridging two aromatic rings *P* and *Q*, passing from the nearest neighbor carbon atom at site *p* to *q*. Here, each carbon atom C_p, or C_q belongs to a different aromatic ring *P* or *Q* which are in the neighbors. (*see* **Figure 1**).

The bridge bond current is given in terms of the interatomic current, $J_{pq}(t)$, as

$$J_{B,pq}(t) = -J_{pq}(t)\,\cos\theta_d. \tag{11}$$

Here, θ_d is the dihedral angle between the two rings *P* and *Q* [39].

We now define an averaged ring current along ring *K*, $J_K(t)$, which is defined by taking the average of all bond currents as

$$J_K(t) \equiv \frac{1}{n_K} \sum_{(i<j)\subset K}^{n_K} J_{ij}(t), \tag{12}$$

where n_K is the number of bonds in ring *K*.

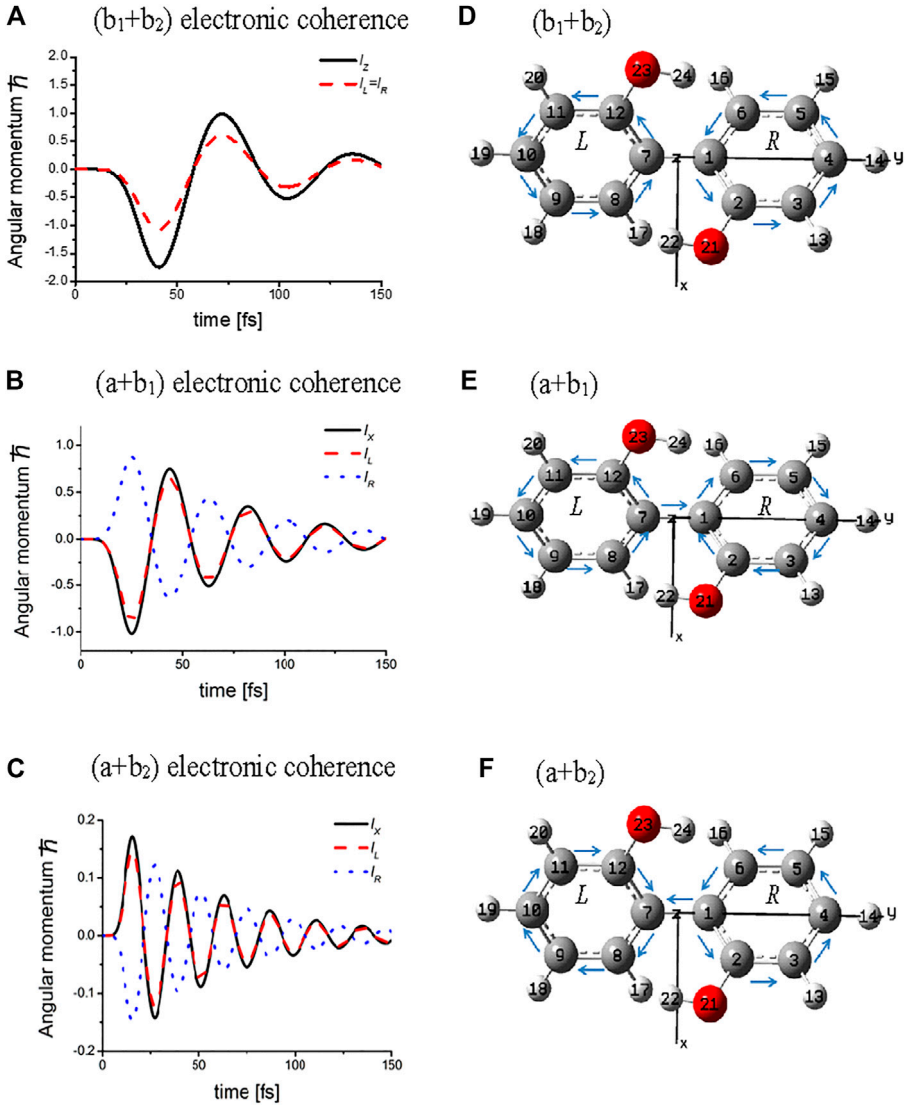

FIGURE 3 | Temporal behaviors of the coherent angular momenta, total values l_Z (l_X), and components, l_L (l_R) of L (R) ring for three types of the electronic coherence and the directions of the bond currents at the initial time: upper panel for ($b_1 + b_2$) electronic coherence excited by laser pulse with amplitude of 0.19 TW/cm^2; middle panel for ($a + b_1$) electronic coherence excited by laser pulse with amplitude of 0.83 TW/cm^2; lower panel for ($a + b_2$) electronic coherence excited by the laser pulse with amplitude of 3.32 TW/cm^2. The dephasing constants were set as $\gamma_{b1b2} = \gamma_{ab1} = \gamma_{ab2} = 0.01$ eV (~1/50 fs^{-1}). The arrows above the C – C bonds indicate the initial directions of the currents. Note that the bridge bond current $J_{1,7} = 0$ for the ($b_1 + b_2$) electronic coherence, while $J_{1,7} \neq 0$ for the ($a + b_1$) and ($a + b_2$) electronic coherences. Reprinted with permission from Ref. [39] Copyright (2013) American Institute of Physics.

2.4 Application to Nonplanar (*P*)-2,2'-biphenol

(*P*)-2,2'-biphenol is one of the typical nonplanar chiral aromatic ring molecules, which has two aromatic rings connected through the C-C bridge bond. For convenience, hereafter, we denote L (R) for the left- (right-) hand side phenol ring of (*P*)-2,2'-biphenol. **Figure 2A** exhibits the geometrical structure of (*P*)-2,2'-biphenol with the transition dipole moments vectors between the ground and excited states. (*P*)-2,2'-biphenol was assumed to be fixed on a surface by a non-conjugated chemical bond or was oriented in the space by the molecular orientation techniques by laser [44–46]. The laboratory-fixed Y-axis was set parallel to the single chemical bond bridging two phenol molecules, and the rotational axis of the molecule belonging to point group C_2 was set along the laboratory-fixed Z-axis which was parallel to the surface normal. The ground state geometry of (*P*)-2,2'-biphenol was optimized using the DFT-B3LYP level theory with the 6-31G+(d,p) basis set in the GAUSSIAN09 code [47]. The dihedral angle θ_d between the two phenol rings, was found to be 108.9° based on the density functional theory (DFT) calculations. The calculated geometrical structures are provided in Refs. [39, 40].

TABLE 1 | Angular momenta of the two phenol rings $l_L \equiv \mathbf{l}_L(t*)\cdot\mathbf{n}_L$ and $l_R \equiv \mathbf{l}_R(t*)\cdot\mathbf{n}_R$, and the resulting angular momenta l_X and l_Z at the maximum coherence time $t = t^{*1)}$.

	$l_L/\hbar$	$l_R/\hbar$	$l_X/\hbar$	$l_Z/\hbar$
$(a+b_1)$	−1.09	1.09	−1.27	0
$(a+b_2)$	0.17	−0.17	0.20	0
(b_1+b_2)	−1.44	−1.44	0	−2.34

1) The maximum coherence occurs at $\mathrm{Im}\,\rho_{b2,b1} = \mathrm{Im}\,\rho_{b1,a} = \mathrm{Im}\,\rho_{b2,a} = -1/2.$ $l_X = 2l_L\cos\frac{\theta_d}{2} = 1.163l_L = -1.163l_R$ *for the* $(a+b_1)$ *or* $(a+b_2)$ *electronic coherences;* $l_Z = 2l_L\sin\frac{\theta_d}{2} = 1.627l_L = 1.627l_R$ *for the* (b_1+b_2) *electronic coherence with dihedral angle* θ_d (= 108.9°) *between the two phenol rings. Reprinted with permission from Ref. [39] Copyright (2013) American Institute of Physics.*

To create the coherent angular momenta and ring currents in (*P*)-2,2'-biphenol, we focused on the three dipole-allowed electronic excited states (a, b_1, and b_2) as shown in **Figure 2B**. The transition energies from the ground (g) to the a, b_1, and b_2 states, which were calculated under the optimized ground state geometry using the TD-DFT B3LYP level of theory [39, 40] were 6.67, 6.78, and 6.84 eV, respectively.

2.4.1 Generation of Two-state Electronic Coherence Using Linearly Polarized UV Pulses

For a creation of the coherent angular momentum and ring current using linearly polarized laser pulses, it is essential to prepare for an electronic coherence with a fixed relative phase between two electronic states, a and b_1, i.e., in-phase ($a + b_1$) or out-of-phase ($a - b_1$). The principle behind the preparation of the electronic coherence ($a + b_1$) (($a - b_1$)) using a linearly polarized laser with polarization unit vector $\mathbf{e}_+$ ($\mathbf{e}_-$) is schematically demonstrated in **Figure 2C** [39, 40].

In the frame work of the three-excited state model, there are three types of two-electronic coherent states represented as $b_1 \pm b_2$, $a \pm b_1$ and $a \pm b_2$, respectively. At the initial time each electronic coherence can be generated by applying a linearly polarized UV laser with a properly selected laser polarized direction. Because of the non-planar geometry of the molecule, the angular momentum is two-dimensional, and the two ring currents flow are on the two different planes, the direction of total angular momentum is dependent on the symmetry of the coherent state created by the laser: The Z-directional angular momentum (ring current) is generated for the created coherent state with the A-irreducible representation of the C_2 point group, while the X-directional angular momentum (ring current) is generated for the coherent state with B.

It is remarkable that even though the third excited state is located between the two excited states in the three-excited states system, the coherent electronic state can still be created if the applied linearly polarized lasers satisfy the following conditions. For example, for the ($a \pm b_2$) electronic coherence, the conditions for the linearly polarized lasers with polarization vectors $\mathbf{e}_\pm$ are given as

$$\boldsymbol{\mu}_{ga}\cdot\mathbf{e}_\pm = \pm\,\boldsymbol{\mu}_{gb2}\cdot\mathbf{e}_\pm \text{ and } \boldsymbol{\mu}_{gb1}\cdot\mathbf{e}_\pm = 0, \tag{13}$$

or equivalently,

$$\mathbf{e}_\pm = \boldsymbol{\mu}_{gb1}\times\left(\boldsymbol{\mu}_{gb2} \mp \boldsymbol{\mu}_{ga}\right)\Big/\left|\boldsymbol{\mu}_{gb1}\times\left(\boldsymbol{\mu}_{gb2} \mp \boldsymbol{\mu}_{ga}\right)\right|. \tag{14}$$

Thus, if the laser overlaps the electronic states a, b_1, and b_2, the ($a + b_2$) or ($a - b_2$) electronic coherent state can be created selectively.

2.4.2 Coherent Angular Momentum Quantum Beats and Bond Currents

Figure 3 exhibits the temporal behaviors of the angular momenta calculated for three types of electronic coherences, (b_1+b_2), (a + b_1) and (a + b_2), each of which is created by a linearly polarized UV laser pulse with a properly selected polarization direction of laser. For the (b_1+b_2) electronic coherence, the total angular momentum parallel to the Z-axis, l_Z, is created together with two ring components $l_L = l_R$, whereas for both the (a + b_1) and (a + b_2) electronic coherences, the total angular momenta parallel to the X-axis, l_X, are generated with $l_L = -l_R$, with a π-phase shift. Similarly, for out-of-phase electronic coherences, ($b_1 - b_2$), ($a - b_1$) and ($a - b_2$), the angular momentum can be given by the corresponding in-phase electronic coherence with a π-phase shift. The simple sinusoidal temporal behavior originates from the coherence of two electronic states with the oscillation period corresponding to a frequency difference between the two-electronic states. This is referred to as the angular momentum quantum beats, which are similar to the fluorescence quantum beats which originate from the vibronic coherence [48]. We note that π-electrons rotate a few times in a unidirectional manner within a half cycle of the oscillation. This unidirectional π-electron rotation can produce a unidirectional ring current and corresponding current-induced magnetic flux. In principle, this enables the design of ultrafast switching devices which consist of organic aromatic ring molecules.

The angular momenta $l_Z(t)$ and $l_X(t)$, shown in **Figure 3**, are obtained by the summation of the angular momenta created in the L and R aromatic rings $\mathbf{l}_L(t)$ and $\mathbf{l}_R(t)$ using the following relationship $l_Z(t) = 2\mathbf{l}_L(t)\cdot\mathbf{e}_Z\sin\frac{\theta_d}{2}$ with $\mathbf{l}_L(t)\cdot\mathbf{e}_Z = \mathbf{l}_R(t)\cdot\mathbf{e}_Z$, and $l_X(t) = 2\mathbf{l}_L(t)\cdot\mathbf{e}_X\cos\frac{\theta_d}{2}$ (where $\mathbf{l}_L(t)\cdot\mathbf{e}_X = -\mathbf{l}_R(t)\cdot\mathbf{e}_X$). **Table 1** lists the angular momenta of (*P*)-2,2'-biphenol with the dihedral angle $\theta_d = 108.9°$ where the electronic coherence is maximum at time $t = t*$, i.e., when the magnitude of the imaginary part of the density matrix element is maximized ($\mathrm{Im}\,\rho_{\alpha\beta}(t*) = -\frac{1}{2}$) and dephasing effects are neglected. This results in $l_X(t*) > 0$ or $l_X(t*) < 0$ for the (a + b_1) and (a + b_2) electronic coherences, respectively, and in $l_Z(t*) < 0$ for the (b_1 + b_2) electronic coherence.

The magnitudes of the bond current, J_{ij} calculated at the maximum coherence time, are presented in detail in [40]. The magnitudes of the averaged ring current over the C-C bonds at the maximum coherence time, $\bar{J}$ are on the order of tens of μA, i.e., $\bar{J}$ = 161, 86.5 and 63.4 μA for (b_1 + b_2), (a + b_1), and (a + b_2) coherences, respectively.

Effects of dephasings on coherent π-electron angular momentum and ring currents were treated in the Markov approximation, and time-independent dephasing constants were used under the assumption of instantaneous interactions between the system and phonon baths. In a system such as condensed phases, the Markov approximation is broken down. Non-Markov

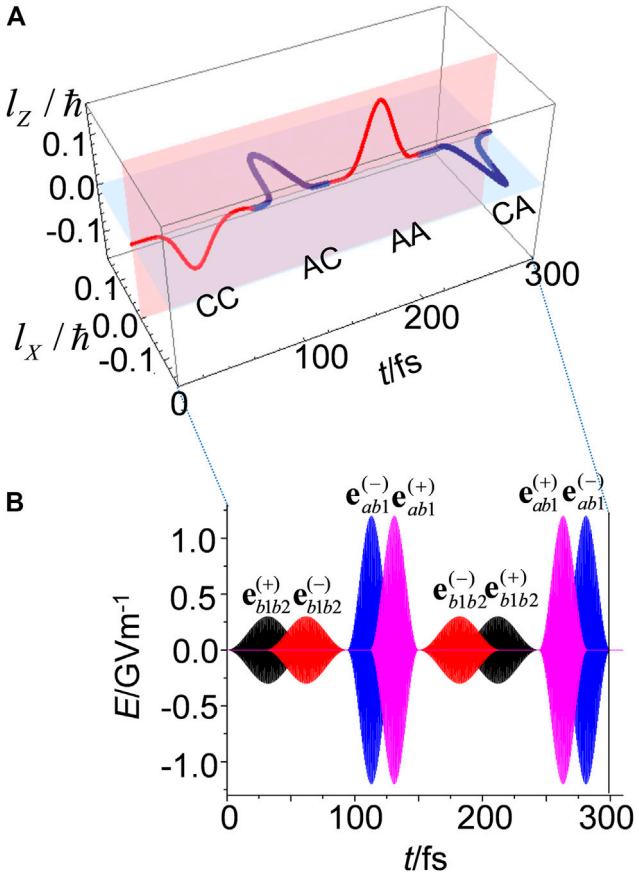

FIGURE 4 | (A) Sequential four-step quantum switching of π-electron rotations in (*P*)-2,2'-biphenol. **(B)** The sequential overlapped pump and dump laser pulses. Reprinted with permission from Ref. [40] Copyright (2012) American Chemical Society.

response of coherent should be essential. Time evolution of coherent ring currents were calculated in a hierarchical master equation approach beyond the Markov approximation has been treated [49].

2.4.3 Ultrafast Quantum Switching of Angular Momentum

Consider the quantum control of π-electron rotations for two-dimensional angular momentum switching based on the results shown in **Table 1**. Here, two-dimensional quantum switching is defined as a sequential pulse of the electronic angular momentum with its constant sign (positive or negative) along the *Z*- or *X*-axis. Note that any quantum switching step should be completed before the reverse rotation of the π-electrons begins, because it may otherwise disturb the signal. Consider a sequential four-step control, which is expressed as $l_Z(-)\rightarrow l_X(+)\rightarrow l_Z(+)\rightarrow l_X(-)$. This indicates the switching of rotational patterns in the order CC → AC → AA → CA, where the symbol C (A) means clockwise (anti-clockwise) direction, and for example, CA rotation means clockwise and anti-clockwise rotations along the phenol rings *L* and *R*, respectively. Here, $l_X(+)$ ($l_Z(-)$) means the π-electron angular momentum along the *X*- (*Z*-) axis with a positive (negative) sign, i.e., anti-clockwise (clockwise) rotation of π-electrons around the corresponding axis.

Figure 4A presents a 3D plot of the angular momentum as it switches based on the sequential four-step control scheme. From **Figure 4A**, we can see that the π-electron rotations are successfully manipulated by the pulses depicted in **Figure 4B**. That is, both the rotational axis parallel to the Z- or X-axis and the rotational directions around those axes, clockwise or anti-clockwise, are manipulated by the sequential four-step process. In **Figure 4B**, each switching step of control was performed using pump and dump pulses with specific polarization directions and phases. The laser pulse with an amplitude of 1.2 GV/m (= 1.9×10^{11} W/cm^2) was used in the second and fourth steps. The dynamic Stark shifts between electronic states *a*, b_1 and b_2 were on the order of 0.01 eV [39], indicating that the Stark effects could be omitted in **Figure 4A**.

The pulses shown in **Figure 4B** have two features. The first feature is that the pump (dump) pulse for each step has polarizations, $\mathbf{e}^{(-)}_{\alpha\beta}(\mathbf{e}^{(+)}_{\alpha\beta})$ or $\mathbf{e}^{(+)}_{\alpha\beta}$ $(\mathbf{e}^{(-)}_{\alpha\beta})$. Each pulse has an energy width that is large enough to coherently excite two quasi-degenerate electronic excited states, as shown in **Figure 2**. The second feature is that the pump

and dump laser pulses partially overlap. In the creation of the CC rotation, for example, the electric field of the pump pulse was $\boldsymbol{E}^{(+)}_{b1b2}(t) = \boldsymbol{e}^{(+)}_{b1b2}E^{0}_{b1b2}\sin^2(\pi t/T_{b1b2})\sin(\omega_{c,b1b2}t)$, while the electric field of the dump pulse was $\boldsymbol{E}^{(-)}_{b1b2}(t) = \boldsymbol{e}^{(-)}_{b1b2}E^{0}_{b1b2}\sin^2(\pi(t-t^{pd}_{b1b2})/T_{b1b2})\sin(\omega_{c,b1b2}t+\pi/2)$. Here, T_{b1b2} (= 60.9 fs) indicates the oscillation period between b_1 and b_2 states, E^{0}_{b1b2} is the amplitude of the laser pulse, $\omega_{c,b1b2}$ is the central frequency between the two excited states b_1 and b_2; and t^{pd}_{b1b2} (the time interval between the pump and dump laser pulses) was set to $T_{b1b2}/2$ (Supporting information in Ref. [39]). The angle between the two polarization vectors, $\mathbf{e}^{(+)}_{b1b2}$ and $\mathbf{e}^{(-)}_{b1b2}$, was 113.5°.

With respect to ultrafast quantum switching, it is crucial to create the overlap of the pump and dump pulses, where the resulting electric field rotates as an elliptically polarized electric field in the overlapped time domain, and the dump laser pulse reverse the rotation that occurs during this region. As a result, the angular momentum of the π-electrons is nullified.

2.4.4 Coherent Ring Current-Induced Magnetic Field

There have been interesting reports on the evaluation of the magnetic fields of atoms and oriented heteronuclear diatomic molecules, AlCl and BeO [32, 50, 51]. Strong and unidirectional magnetic fields are generated from the degenerate electronic states of these atoms and molecules excited by circularly polarized intense laser pulses. We estimated the magnetic fields (magnetic field flux density) generated by the coherent ring currents of (*P*)-2,2'-biphenol. The results may provide fundamental information for designing ultrafast switching devices controlled by current-induced magnetic fields as well as coherent ring currents [52–54].

As an example, consider the magnetic field induced by the ring current for the (b_1 + b_2) electronic coherence. In **Figure 5**, $B_K(t*,h)$ represents the current-induced magnetic field along the central axis perpendicular to ring *K* (*L* or *R*) as a function of the height *h* above the Z-axis at $t = t*$ under the maximum coherence condition (when Im $\rho_{b_1b_2}(t*) = -1/2$). An expression for the magnetic field $B_K(t*,h)$ was derived by taking into account the interatomic bond currents with the $2p_z$ Slater AOs [40]. Note that $B_L(t*,h) = B_R(t*,h)$ for the (b_1 + b_2) electronic coherence (**Table 1**). It is interesting to compare the behaviors of $B_K(t*,h)$ with those calculated using

$$B^{SRL}_{K}(t,h) = \frac{\mu_0 J_K(t)}{2r}\sin^3\eta, \tag{15}$$

which was derived using a simple ring loop (SRL) model. Here, $\mu_0 = 4\pi\cdot 10^{-7}\,[\mathrm{W}_b/(\mathrm{A}\cdot\mathrm{m})]$ is the magnetic constant, r (= r_{ij}) is the ring radius, and η (= $\sin^{-1}(r/\sqrt{r^2+h^2})$) is defined as the angle between the Z-axis and a straight line depicted from the point on ring *K* that crosses the Z-axis. $B_K(t,0)$ at $\eta = \pi/2$ is the magnetic field measured at the center of ring *K*. The magnitude of $B_K(t^*,0)$ induced by $J_K(t^*)$ = 100 μA is 448 mT at the center of the ring *K* with r = 0.14 nm. It can be found from **Figure 5** that the magnitudes of $B^{SRL}_{K}(t^*,h)$ are overestimated near the aromatic ring plane $0 \le h < 1$ Å, while the magnitudes are reasonable for $h > 1$ Å, although slightly different results can be observed between the two magnetic fields for large values of *h*. At the center of the aromatic ring, $B_K(t^*,h=0) = 0.66B^{SRL}_{K}(t^*,h=0)$. This can be understood from the result that the π-electron current density is densely distributed over the aromatic ring. A subtle difference between $B^{SRL}_{K}(t*,h)$and $B_K(t*,h)$ is observed for large *h*, although both magnetic fields $B^{SRL}_{K}(t*,h\to\infty) = 0$ and $B_K(t*,h\to\infty) = 0$ approach zero. This deviation originates from the approximation that the aromatic ring is not a considered to be a perfect ring.

It is necessary to check whether the value of $B_K(t,0)$ is larger than the one corresponding to the magnetic field B_{Laser} induced by the applied laser field *F* when the induced magnetic fields are created during an ultrasfast laser pulse excitation at the early time regime. The magnitude of magnetic field B_{Laser} can be estimated from a simple formula $|B_{\mathrm{Laser}}| = |F|/c$ with $c = 3.0\times10^{8}\,\mathrm{ms}^{-1}$. The calculated magnitude of magnetic field B_{Laser} with $|F|$ = 1.0 GV/m is approximately $7.4B_K(t*,h)$, which is on the same order as the field induced by the ring current J = 100 μA. This implies that we need a careful examination to observe the current-induced magnetic flux, or to use the electro-magnetic device as a switching control tool.

Thus far, we have taken into account the ring current-induced magnetic fields of the low-symmetry aromatic ring molecule (*P*)-2,2'-biphenol, in which nondegenerate two electronic excited states are coherently excited by the linearly polarized UV lasers. Here we briefly discuss the ring current-induced magnetic field for the *degenerate* electronic excited states of an aromatic molecule induced by the intense *circularly polarized* UV laser pulse. Yuan and Bandrauk [2, 33] have numerically demonstrated that the circularly polarized ultrashort pulses are generated from the molecular high-order harmonic generation using the intense linearly and circularly polarized laser pulses. This indicates a possibility for the ultrashort circularly polarized UV laser pulses to create the ring current-induced magnetic fields in high symmetric aromatic ring molecules. We can estimate the magnitude of the ring current-induced magnetic field of benzene within the SRL model using **Eq. 15**. Here, $J(t)$ is the electric ring current of the degenerated electronic state. The electronic spectrum of benzene is characterized by the dipole-allowed transition from the ground state to the third singlet electronic excited state ($^1\mathrm{E}_{1u}$). For an equal population between the two states at $t = t*$, $B^{SRL}(t*,0) = 874$ mT is obtained using the maximum value of the coherent ring current $J(t*) = 195$ μA evaluated under the π-electron approximation [40, 55]. For comparison, we obtained $B^{SRL}_{K}(t*,0) = 874$ mT and $B_K(t*,0) = 579$ mTwhen $J(t*) = 195$ μAfor (*P*)-2,2'-biphenol. Note that the same magnitudes of the induced magnetic field $B^{SRL}_{K}(t*,0)$ for (*P*)-2,2'-biphenol and $B^{SRL}(t*,0) = 874$ mT for benzene were obtained in the SRL model because the two parameters in the SRL model, the radius of the ring *r*, and the ring current $J(t^*)$ have the same values for both types of ring molecules. The same tendency in the magnitudes between $B^{SRL}_{K}(t^*,0)$ and $B_K(t^*,0)$ is also observed for benzene.

3 CURRENT LOCALIZATION IN POLYCYCLIC AROMATIC HYDROCARBONS

In this section we consider a localization of coherent ring current in polyatomic aromatic hydrocarbons (PAH) [41, 42]. There exist

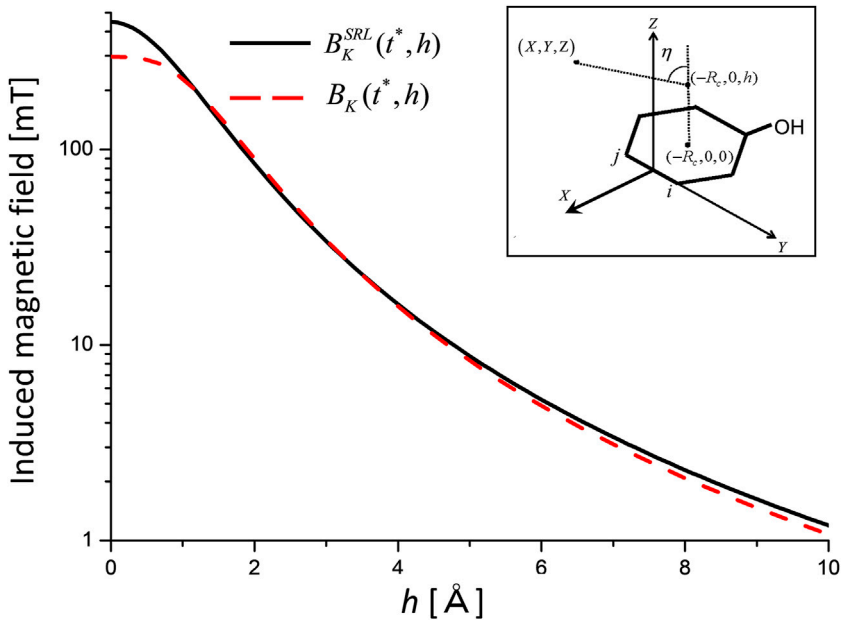

FIGURE 5 | Induced magnetic fields for the (b_1 +b_2) electronic coherence as a function of height h measured from the center of aromatic ring K at the maximum coherence time $t = t*$. $B_K^{SRL}(t*,h)$ and $B_K(t*,h)$ represent the induced magnetic field calculated by a simple ring loop model, and the field calculated by the expression that explicitly takes into account the coherent ring currents, respectively. The inset panel defines the coordinate system for height h and angle η. R_c denotes the center of the phenol ring.

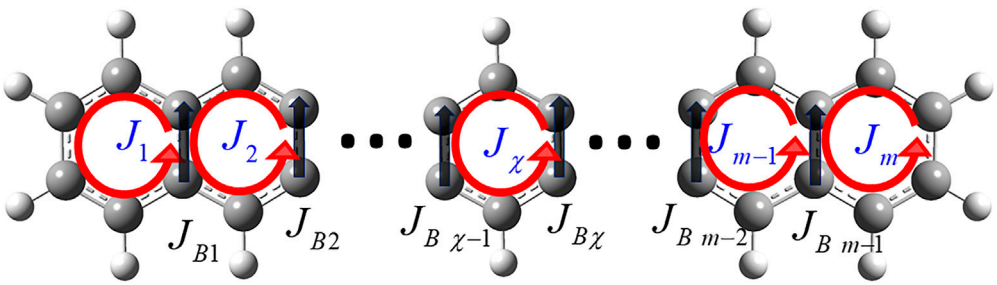

FIGURE 6 | π-Electron ring currents J_l and bridge bond currents $J_{Bl'}$ ($1 \le l \le m$, $1 \le l' \le m-1$) in a linear planar polycyclic aromatic hydrocarbon (PAH). J_χ refers to the π-electron ring current localized on aromatic ring χ.

various current localization patterns in PAH simply because of their geometrical structures consisting of many benzene units. Quantum optimal control method is a general and reliable one to choose a desired current localization pattern from the various patterns using control lasers. The quantum control method has successfully been applied to manipulation of molecules such as coherent control of chemical reactions [56, 57]. After a brief introduction of quantum optimal control method [41, 42, 58], we demonstrate how the target state is set up for the designated ring current using the Lagrange multiplier method. Here, the π-electron ring current is expressed in terms of the interatomic bond currents between two adjoining C–C atoms. At final, the target states are derived for the two types of current localization: the localized ring current, which indicates that the ring current is localized to the designated aromatic ring in linear PAH, and the perimeter ring current in linear PAH [41, 42].

3.1 Quantum Optimal Control Approach

The objective functional to be maximized, is defined as [59–61].

$$J[\mathbf{F}] = \left\langle \Psi(T)\middle|\hat{O}_T\middle|\Psi(T)\right\rangle - \alpha_0 \int_0^T dt\,(\mathbf{F}(t))^2 - 2\,\mathrm{Im}\left[\int_0^T dt \left\langle \xi(t)\middle| i\hbar\frac{\partial}{\partial t} - (H_0 - \boldsymbol{\mu}\cdot\mathbf{F}(t))\middle|\Psi(t)\right\rangle\right], \quad (16)$$

where H_0 is a Hamiltonian in absence of field, and $\Psi(t)$ is the time-dependent wave function in the electric field $\mathbf{F}(t)$. Here, the

target operator $\widehat{O}_T$ is expressed as $\widehat{O}_T = |\Psi_T > < \Psi_T|$, where Ψ_T is the target state wave function at the final time T, defined as $\Psi_T = \sum_a c_a(T)\Phi_a$, and is equal to $\Psi(T)$ under the optimal condition, $\widehat{O}_T = |\sum_a c_a(T)\Phi_a\rangle\langle\sum_b c_b(T)\Phi_b|$. The penalty factor α_0 is introduced to suppress the magnitude of the electric field $\mathbf{F}(t)$. $\xi(t)$is the time-dependent Lagrange multiplier. The third term in **Eq. 16** is added to decouple the boundary conditions of the equations for $\Psi(t)$ and $\xi(t)$ as indicated in **Eq. 17.** Taking the variational condition $\delta J[\mathbf{F}] = 0$, the following coupled equations are obtained,

$$i\hbar\frac{\partial}{\partial t}\Psi(t) = \big(H_0 - \boldsymbol{\mu}\cdot\mathbf{F}(t)\big)\Psi(t), \tag{17a}$$

$$i\hbar\frac{\partial}{\partial t}\xi(t) = \big(H_0 - \boldsymbol{\mu}\cdot\mathbf{F}(t)\big)\xi(t), \tag{17b}$$

where

$$\mathbf{F}(t) = -\frac{1}{\alpha_0}\mathrm{Im}\langle\xi(t)|\boldsymbol{\mu}|\Psi(t)\rangle. \tag{17c}$$

Here, $\Psi(t)$ satisfies the initial condition $\Psi(0) = \Phi_0$, and $\xi(T)$ satisfies the condition, $\xi(T) = \widehat{O}_T\Psi(T)$ at final time T. Note that by solving **Eq. 17**, we obtain the optimal solution $\Psi(T)$, which is equal to Ψ_T.

3.2 Setup of Target Operators

Consider the ring current localization to a designated ring χ in a PAH, as shown in **Figure 6**. From **Eqs. 10a**, **12**, the ring current on ring κ at the target time T is expressed as

$$\begin{aligned} J_\kappa(T) &\equiv \frac{1}{n_\kappa}\sum_{\alpha=1}^{n}\sum_{\beta=1}^{n}\sum_{(i<j)\subset\kappa}^{n_\kappa} J_{ij,\alpha\beta}(T) \\ &= \sum_{\alpha=1}^{n}\sum_{\beta=1}^{n} J_{\kappa,\alpha\beta}\mathrm{Im}\big(c_\alpha(T)c_\beta^*(T)\big) \\ &= J_\kappa(c_1, c_2, \cdots c_n),\ (1\le\kappa\le m) \end{aligned} \tag{18a}$$

with $c_i \equiv c_i(T)$, and

$$J_{\kappa,\alpha\beta} = \frac{2n_e e\hbar}{m_e}\sum_{(i<j)\subset\kappa}^{n_\kappa}\Big\{\Big(\delta_{ab}\big(c_{a'i}^* c_{b'j} - c_{b'i}^* c_{a'j}\big) + \delta_{a'b'}\big(c_{ai}^* c_{bj} - c_{bi}^* c_{aj}\big)\Big)J_{ij}\Big\}. \tag{18b}$$

Here, n is the number of electronic excited states. Hereafter, we write $c_\alpha(T)$ as c_α for simplicity.

The target state $\Psi_T = \sum_\alpha c_\alpha\Phi_\alpha$ can be determined by applying the Lagrange multiplier method to the ring currents at the target time T in **Eq. 18a**, which provides the coupled equations in terms of the configuration interaction coefficients with $\{\mathrm{Re}c_\alpha, \mathrm{Im}c_\alpha\}$. The target operator is given as $\widehat{O}_T = |\Psi_T > < \Psi_T|$.

The coupled equations for the ring current localization to aromatic ring χ can be expressed as

$$\sum_{\beta=1}^{n} J_{\chi,\beta\alpha}\mathrm{Im}c_\beta + \sum_{\kappa\neq\chi}^{m}\sum_{\beta=1}^{n}\lambda_\kappa J_{\kappa,\beta\alpha}\mathrm{Im}c_\beta + \lambda_\chi\mathrm{Re}c_\alpha = 0,\ (1\le\alpha\le n) \tag{19a}$$

$$-\sum_{\beta=1}^{n} J_{\chi,\beta\alpha}\mathrm{Re}c_\beta - \sum_{\kappa\neq\chi}^{m}\sum_{\beta=1}^{n}\lambda_\kappa J_{\kappa,\beta\alpha}\mathrm{Re}c_\beta + \lambda_\chi\mathrm{Im}c_\alpha = 0,\ (1\le\alpha\le n) \tag{19b}$$

$$\sum_{\alpha=1}^{n}\big((\mathrm{Re}c_\alpha)^2 + (\mathrm{Im}c_\alpha)^2\big) - 1 = 0, \tag{19c}$$

and

$$\sum_{\beta=1}^{n}\sum_{\alpha=1}^{n} J_{\kappa,\alpha\beta}\big(\mathrm{Im}c_\alpha\mathrm{Re}c_\beta - \mathrm{Re}c_\alpha\mathrm{Im}c_\beta\big) = 0\,. \tag{19d}$$

A brief derivation of **Eq. 19** is summarized in **Appendix A**.

The coefficients $\{\mathrm{Re}c_\alpha, \mathrm{Im}c_\alpha\}$with λ_l included are numerically determined by applying the Newton-Raphson method to the coupled equations in **Eq. 19**. The target operator for the localization is obtained as $\widehat{O}_T = |\sum_\alpha c_\alpha\Phi_\alpha\rangle\langle\sum_\beta c_\beta\Phi_\beta|$.

Now consider the bridge bond currents $J_{Bl'}$ shown in **Figure 6**, and the perimeter ring current of a PAH with m aromatic rings, $J_P \equiv \frac{1}{m}\sum_{l=1}^{m} J_l$, which is defined as the average of the π-electron ring currents at each aromatic ring site. For the perimeter ring current, the bridge bond currents $J_{Bl'}(1\le l'\le m-1)$ flowing among the nearest neighbor aromatic rings, should be zero at the target time. The target operators for the bridge bond currents, $J_{Bl'}(1\le l'\le m-1)$, and perimeter ring current, J_P, can be derived from **Eq. 19** by replacing $J_{\kappa,\beta\alpha}$ with $J_{Bl',\beta\alpha}$ and $J_{P,\beta\alpha}$, respectively, because $J_{Bl'}$ and J_P can be written in terms of $\{\mathrm{Re}c_\alpha, \mathrm{Im}c_\alpha\}$ as

$$J_P = \sum_{\beta=1}^{n}\sum_{\alpha=1}^{n} J_{P,\alpha\beta}\big(\mathrm{Im}\,c_\alpha\,\mathrm{Re}c_\beta - \mathrm{Re}c_\alpha\,\mathrm{Im}\,c_\beta\big), \tag{20a}$$

and

$$J_{Bl'} = \sum_{\beta=1}^{n}\sum_{\alpha=1}^{n} J_{Bl',\alpha\beta}\big(\mathrm{Im}\,c_\alpha\,\mathrm{Re}c_\beta - \mathrm{Re}c_\alpha\,\mathrm{Im}\,c_\beta\big), \tag{20b}$$

respectively.

Similar to **Eq. 19**, the coupled equations for the perimeter ring current are derived in **Appendix B**.

3.3 Application of Current Localization Control to Anthracene

We applied the quantum optimal control (QOC) method described in the preceding section to anthracene, one of the smallest PAHs [42]. Anthracene (D_{2h}) was assumed to be fixed on a surface (the XY plane), or oriented spatially by lasers The molecular geometry was optimized in the MP2/6-311+g(d,p) level theory using the GAUSSIAN09 code [47]. As demonstrated in **Figure 7A**, anthracene consists of three aromatic rings, which are called *L*-, *M*-, and *R*- rings respectively.

Consider the two types of π-electron localized ring currents of anthracene: the perimeter current flowing along the outside chemical bonds of anthracene, and the middle ring current localized to the *M*-ring. Both types of localized ring currents belong to the irreducible representation B_{1g} of the D_{2h} point group, which are symmetry-adapted. The excited states contributing to the two ring currents need to belong to the B_{3u} and B_{2u} representations, because each corresponding electronic coherence created by the two excited states belongs to the B_{1g} representation. The excited state for the localized ring

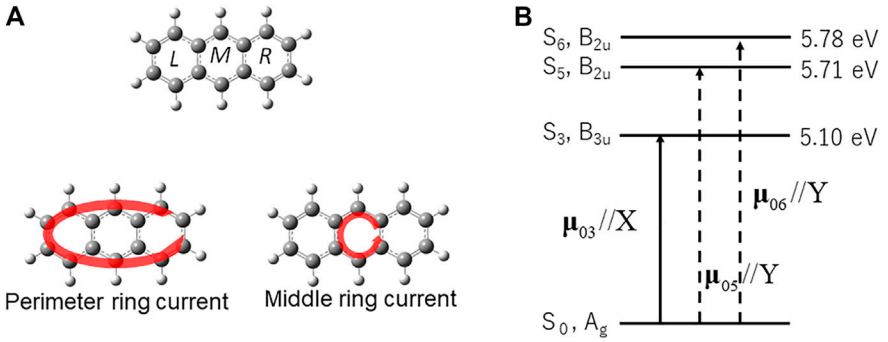

FIGURE 7 | (A) Symmetry-adapted ring currents (B_{1g}) in anthracene, perimeter ring current, and middle ring current. **(B)** The electronic excited states adapted for laser control of π-electron ring in anthracene (D_{2h}), and the non-zero transition dipole moments between the ground/excited-excited states. The solid (dashed) arrows represent the transition dipole moments which are parallel to the X (Y) axis.

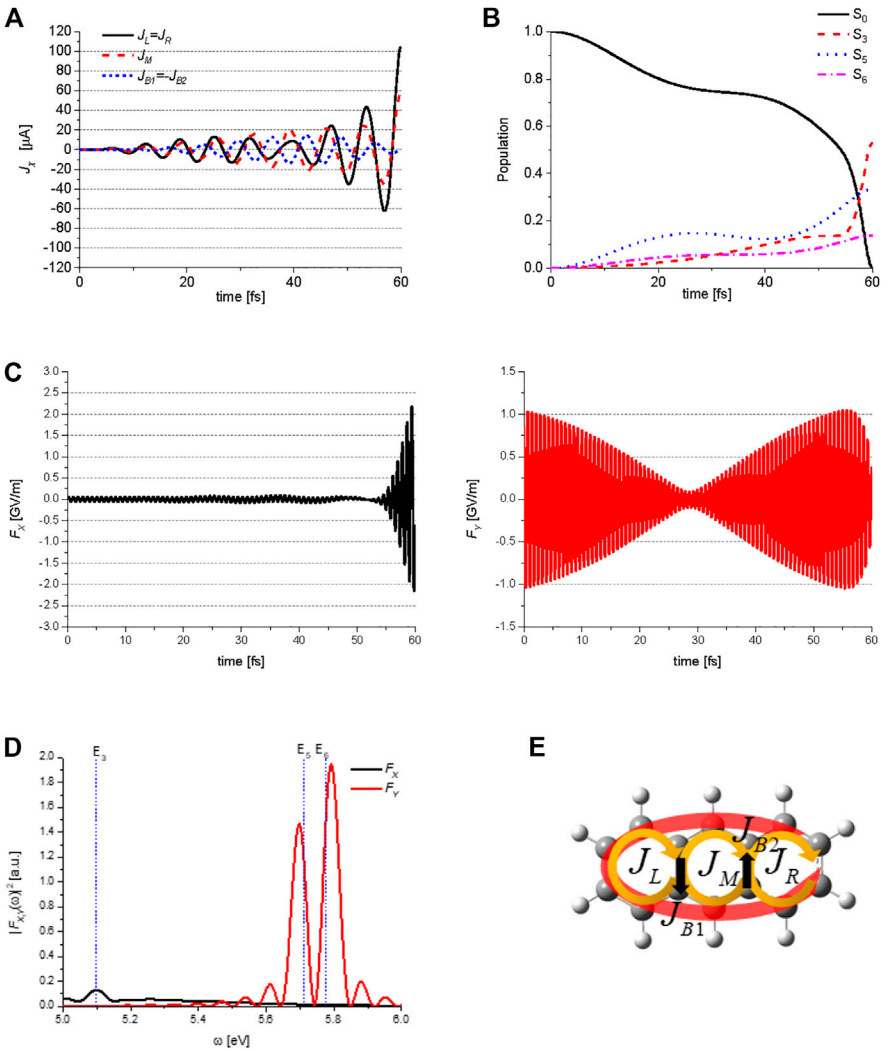

FIGURE 8 | Quantum optimal control simulations for generation of the perimeter ring current in anthracene: **(A)** temporal behavior of the three ring currents $J_L(t) = J_R(t)$ (solid line), $J_M(t)$ (broken line), and those of the two bridge bond currents $J_{B1}(t) = -J_{B2}(t)$ (dotted line); **(B)** temporal behavior of the population in S_0, and those in the three excited states: $S_3(B_{2u})$, $S_5(B_{2u})$, and $S_6(B_{2u})$; **(C)** optimized *X*- polarized laser pulse field $F_X(t)$ **(left-hand side)** and *Y*-polarized $F_Y(t)$ **(right-hand side)**; **(D)** Fourier transformed spectra of the two laser fields $F_X(\omega)$ and $F_Y(\omega)$; **(E)** five components of the perimeter ring current at an arbitrary time. Reprinted with permission from Ref. [40] Copyright (2012) American Chemical Society.

TABLE 2 | Matrix elements of the coherent π-electron ring currents for the three aromatic rings of anthracene, $J_{x,\alpha\beta}(X = L, M, R)$, and those of the coherent bond currents shared by the two adjacent aromatic rings, $J_{Bi,\alpha\beta}$ (i = 1, 2) (*see* **Figure 8E**).

α	β	$J_{L,\alpha\beta}$ (μA)	$J_{M,\alpha\beta}$ (μA)	$J_{R,\alpha\beta}$ (μA)	$J_{B1,\alpha\beta}$ (μA)	$J_{B2,\alpha\beta}$ (μA)
S_3 (B_{3u})	S_5 (B_{2u})	82.2	80.8	82.2	−32.5	32.5
S_3 (B_{3u})	S_6 (B_{2u})	65.4	−18.0	65.4	49.0	−49.0

L (R) indicate the left (right)-hand side ring, M corresponds to the middle ring. Here a positive current denotes that the ring current flows (the π-electron rotates) in an anti-clockwise (clockwise) direction. Reprinted with permission from Ref. [42] Copyright (2017) American Institute of Physics.

current is S_3 with B_{3u} representation, and the other two excited states S_5 and S_6 with B_{2u} representation as shown in **Figure 7B**. This defines a "symmetry-adapted ring current" [41, 42].

The excited state energies in **Figure 7B** were calculated to be $E_3 = 5.10$ eV, $E_5 = 5.71$ eV, and $E_6 = 5.78$ eV. Here, S_4 (B_{3u}) with $E_4 = 5.13$ eV was excluded because the oscillator strength was negligibly small (f = 0.0013) in our numerical simulation. The non-zero transition dipole moments relevant to the coherent π-electron ring current control were calculated using the time-dependent density functional theory (TDDFT) method as, $\boldsymbol{\mu}_{S0,S3} = (-3.98, 0, 0)$, $\boldsymbol{\mu}_{S0,S5} = (0, -0.64, 0)$, and $\boldsymbol{\mu}_{S0,S6} = (0, -0.44, 0)$ (in a.u.) for the ground and excited states. The vapor absorption spectrum of anthracene shows the strongest absorption peak at 5.30 eV [62], which corresponds to $E_3 = 5.10$ eV in the TDDFT calculation.

Figure 8 shows the QOC results for the generation of an anti-clockwise perimeter ring current in anthracene. The target state is expressed from the results obtained using the Lagrange multiplier method as

$$\Psi_{AAA} = 0.717i\Phi_{S3} + 0.581\Phi_{S5} + 0.385\Phi_{S6}. \quad (21)$$

Here, the subscripts specifying the target state, for example, ACA for Ψ_{ACA}, indicates the anti-clockwise ring currents in two aromatic rings, L and R, and a clockwise ring current in aromatic ring M. It should be noted that the target state for a generation of any coherent ring current is expressed in terms of its complex form. The control target time was set to $T = 60$ fs. The matrix elements of π-electron ring currents $J_{X,\alpha\beta}$ ($X = L, M, R$) and the bond current $J_{Bi,\alpha\beta}$ (i = 1, 2), for two excited states α, β are presented in **Table 2**. Here the π-electron ring current flowing in an anticlockwise direction is defined as positive, whereas the bond current flowing toward the Y direction is defined as positive (*See* **Figure 6**). **Figure 8A** shows the temporal evolutions of the coherent ring currents J_χ for the three aromatic rings of anthracene, $\chi = L$, M, R, and those for $B1$ and $B2$. It can be observed from **Figure 8A** that the two bond currents $J_{B1,\alpha\beta}$ and $J_{B2,\alpha\beta}$ vanish at the target control time of $T = 60$ fs, and all ring currents in three aromatic rings exhibit positive. This indicates that the coherent π-electrons rotate clockwise along the outside (perimeter) of the aromatic ring. The laser-controlled π-electrons includes a ring current averaged over the three aromatic rings, $J_p \equiv (J_L + J_M + J_R)/3 = 89.0$ μA, which is the perimeter ring current.

Figure 8B shows the temporal behavior of the ground state S_0, and three excited states S_3 (B_{3u}), S_5 (B_{2u}), and S_6 (B_{2u}) populations during the QOC process, which are induced by the two control lasers. **Figure 8C** shows the X and Y-components of the electric field $\mathbf{F}(t)$ generated by the control lasers, and **Figure 8D** shows the Fourier transformed spectra $F_X(\omega)$ and $F_Y(\omega)$ in the ultraviolet (UV) frequency domain. By analyzing the temporal behavior of the electric field $\mathbf{F}(t)$ of the control lasers in **Figure 8C** and the Fourier transformed spectra of the control laser fields in **Figure 8D**, the mechanisms of the laser-controlled ring currents in anthracene can be clarified. It is evident that from the modulation in **Figure 8C** the two linearly (Y-) polarized lasers with a relative phase zero induce the electronic coherence between the two excited states S_5 (B_{2u}) and S_6 (B_{2u}), and that the linearly polarized laser pulse parallel to the X-axis creates the perimeter ring current on the molecular plane.

Thus far, we have considered the QOC procedure for generating an anti-clockwise perimeter current. The QOC procedure for generating a clockwise perimeter current can be carried out in the same manner as described above (*See* **Eq. 21**) by considering the target state,

$$\Psi_{CCC} = \Psi^*_{AAA} = -0.717i\Phi_{S3} + 0.581\Phi_{S5} + 0.385\Phi_{S6}. \quad (22)$$

We carry out the QOC procedure to generate the anticlockwise ring current localized to the middle ring of anthracene. The target state is expressed as

$$\Psi_{0A0} = 0.707\Phi_{S3} - 0.440i\Phi_{S5} + 0.553i\Phi_{S6}. \quad (23)$$

The target state for the middle ring current with the clockwise flow is given by the relationship $\Psi_{0C0} = \Psi^*_{0A0}$. **Figure 9** exhibits the QOC results, where **Figure 9A** displays the temporal evolutions of ring current localization control to the three aromatic rings, indicating that J_M is a ring current with 64.4 μA at the target control time of 60 fs, but on the other hand the ring currents J_L and J_R of the other two aromatic rings vanish. This indicates that the ring current localized to the middle aromatic ring is created by the control laser pulses presented in **Figures 9C,D**. The temporal behaviors of the populations shown in **Figure 9B** are nearly the same as those of the perimeter ring currents as shown in **Figure 8B**. As presented in **Figure 9C**, the two linearly (Y-) polarized lasers induce the electronic coherence between the two excited states S_5 and S_6 with a definite relative phase π, in contrast to the results presented in **Figure 8C**. In the mechanism of generation between the perimeter and the middle ring currents there is no difference except the phase difference between the two excited states S_5 and S_6, because the temporal behavior in both **Figure 8B** and **Figure 9B** and the temporal behavior in the X-polarized laser pulse in both **Figure 8C** and **Figure 9C** are similar to each other.

Main difference between the temporal behaviors of the Y-polarized lasers in **Figure 8C** and **Figure 9C** can be explained briefly in the following. The two coherent states created by the Y-polarized lasers can be expressed as

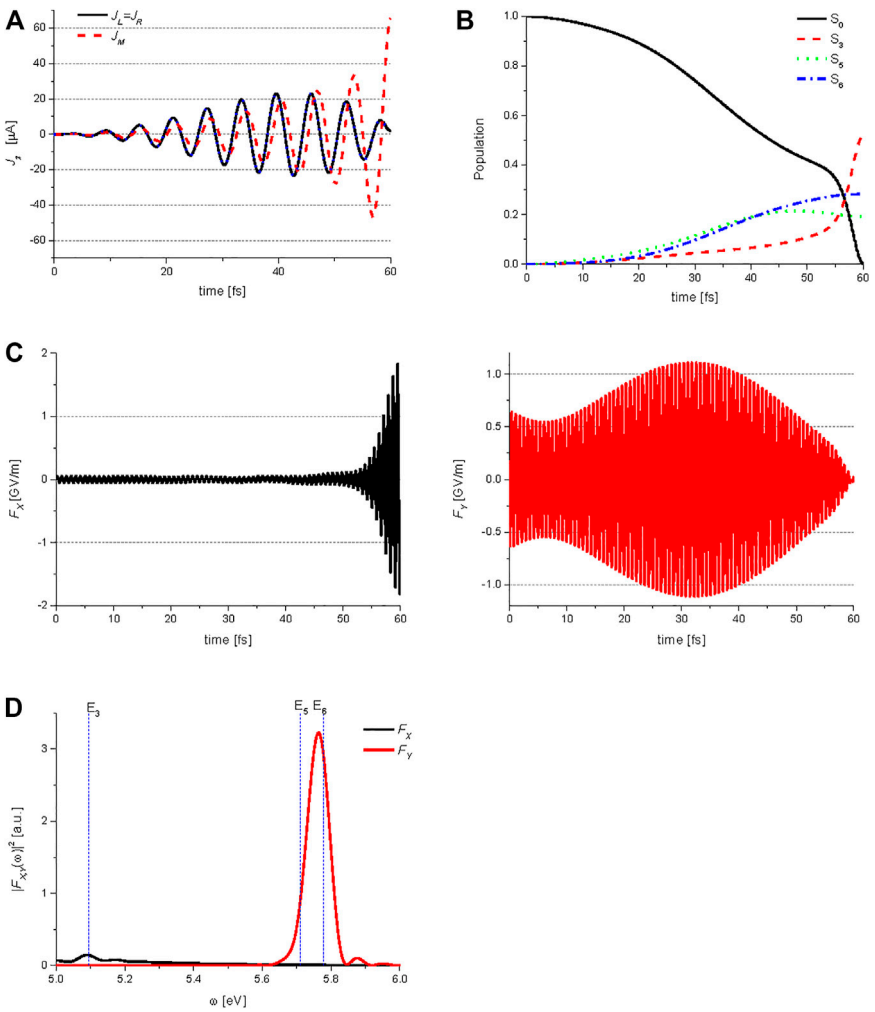

FIGURE 9 | Quantum optimal control simulations for generation of the middle ring current in anthracene: **(A)** temporal behavior of the ring currents $J_L(t) = J_R(t)$ (solid line) and $J_M(t)$ (broken line); **(B)** temporal behavior of the S_0 population and those of the three excited state $S_3(B_{2u})$, $S_5(B_{2u})$ and $S_6(B_{2u})$ populations; **(C)** optimized *X*- and *Y*-polarized laser pulse fields $F_X(t)$ **(left-hand side)** and $F_Y(t)$ **(right-hand side)**; **(D)** Fourier transformed spectra of the laser pulse fields $F_X(\omega)$ and $F_Y(\omega)$. Reprinted with permission from Ref. [42] Copyright (2017) American Institute of Physics.

$$F_+(t) = F_{S5}\ sin(\omega_{S5}t) + F_{S6}\ sin(\omega_{S6}t), \tag{24a}$$

and

$$F_-(t) = F_{S5}\ sin(\omega_{S5}t) - F_{S6}\ sin(\omega_{S6}t). \tag{24b}$$

For simplicity, the amplitudes of the two coherent states are assumed to have the same value, i.e., $F_{S5} = F_{S6} \equiv F_Y$. The above expressions can then be simplified to

$$F_+(t) = F_Y sin\left[\frac{(\omega_{S5} + \omega_{S6})t}{2}\right]\cos\left[\frac{(\omega_{S5} - \omega_{S6})t}{2}\right], \tag{25a}$$

and

$$F_-(t) = F_Y cos\left[\frac{(\omega_{S5} + \omega_{S6})t}{2}\right]\sin\left[\frac{(\omega_{S5} - \omega_{S6})t}{2}\right]. \tag{25b}$$

Here, the frequency difference $|\omega_{S5} - \omega_{S6}|/2$ yields an oscillation beating period of 120 fs, which is nearly the same as that of the quantum beat frequency observed in **Figure 8C** and **Figure 9C**.

Having clarified the control mechanism of the coherent ring current generation, we can semi-quantitatively reproduce the above results in **Figures 8**, **9** by using an analytical method [42]. This indicates, in principle, that two types of ring current localizations, the perimeter ring current and the middle ring current in linear PAHs, can be generated in experiment using three coherent UV lasers without a sophisticated QOC device.

For QOC numerical simulations of the ring current localization control in anthracene, we have only considered the perimeter and the middle ring currents generations, which are symmetry-adapted, while we did not consider a ring current localization to the *L*- or *R*-ring of anthracene, which are created by a symmetry-broken procedure, as demonstrated for naphthalene in Ref. [41]. That is, other excited state(s) with gerade symmetry must be considered in addition to the excited

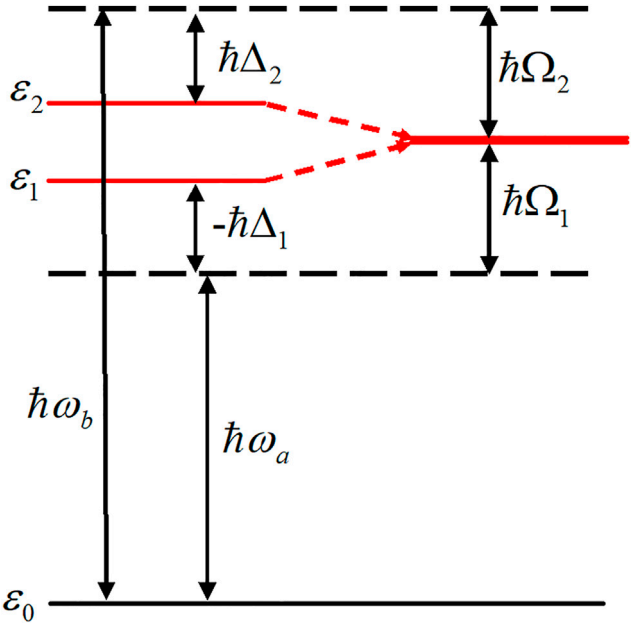

FIGURE 10 | Dynamic Stark-induced degenerate state with the Rabi frequencies (Ω_1 and Ω_2) using two stationary linearly-polarized lasers with the frequencies, ω_a and ω_b, and detuning frequencies Δ_1 andΔ_2 respectively.

states with ungerade symmetry as described in the previous subsection.

It is important to consider how to observe the ultrafast coherent ring currents in PAHs. We proposed a method to detect the direction of the atto-second coherent ring current by tracking the femtosecond molecular vibrational motions that can induce the nonadiabatic couplings [30]. Rodriguez and Mukamel [63] have proposed measuring the circular dichroism (CD) of the ring current using the pump-probe method. Recently, two methods have been proposed for the detection of the ultrafast coherent ring currents. One method, recently proposed by Yuan et al., Bandrauk's group [64], is utilizing the atto-second detection method of the coherent electronic dynamics in molecules with the temporal and spatial resolutions using the circularly polarized ultrashort UV pump and X-ray probe laser pulses. The other method is to utilize the time-resolved scanning microscopy (STM) and the magnetic force microscopy (MFM) to detect the ring current-induced magnetic fields during the ultrashort time [65–67].

It is also expected that to apply our methods to planar or non-planar extended molecular systems, such as graphene sheets. In principle, our method can be extended to these large systems, by considering the symmetry of the molecular system and the constraints on the π-electron ring currents.

Using laser control, it is also essential to maintain the created ring current at the target region (path) at least during one vibrational period of the PAH [68]. Otherwise, the created ring current would dissipate quickly because of the vibronic interactions and/or the nonadiabatic couplings between the two electronic excited states [30, 69–71].

4 DYNAMIC STARK-INDUCED π-ELECTRON ROTATIONS IN LOW-SYMMETRY AROMATIC RING MOLECULES

In this section, we present a convenient method for inducing unidirectional π-electron rotations in aromatic ring molecules with low symmetry [43]. The basic idea behind the induction of unidirectional electron rotations is to degenerate two nondegenerate excited states by utilizing dynamic Stark shifts, as demonstrated in **Figure 10**. We refer to this as the dynamic Stark-induced degenerate electronic state (DSIDES) [43]. Two linearly polarized continuous lasers operating at different frequencies and phases are used to form DSIDES: Each laser is set to selectively interact with each electronic state through non-resonant excitation. The lower and higher excited states are shifted up and down with the same population, respectively, and the DSIDES is formed at the center between them. As a result, unidirectional π-electron rotation is driven by two lasers. In the laser control scenario, only one input parameter out of the four possible parameters (frequency and intensity for each laser), is required to induce the DSIDES formation.

First, the DSIDES formation is described in a three-electronic state model under the fixed nuclei condition, and the time-dependent expectation value of the angular momentum operator of π-electrons is derived and analytically expressed. Next, to demonstrate the applicability of the control scenario, the results of the DSIDES treatment for toluene, which is a typical aromatic ring molecule of low symmetry belonging to Cs point group, are presented.

4.1 Formation of Dynamic Stark-Induced Degenerate Electronic State DSIDES and the Resulting Angular Momentum

Consider the coherent π-electron angular momentum in an aromatic ring molecule with low symmetry excited by non-resonant, stationary UV/visible lasers. The molecule of our interest is one oriented in a space or attached to a surface, as mentioned in the preceding sections. We adopt a three-electronic state model in the frozen nuclei approximation. The three electronic states including the ground state specified by the energy $\varepsilon_0\,(\equiv \hbar\omega_0)$, and two excited states specified by $\varepsilon_1\,(\equiv \hbar\omega_1)$ and $\varepsilon_2\,(\equiv \hbar\omega_2)$, as shown in **Figure 10**. Here, DSIDES can be formed by two stationary linearly polarized lasers with detuning frequencies $\Delta_1 = \omega_a - \omega_{10} < 0$ and $\Delta_2 = \omega_b - \omega_{20} > 0$. The frequency difference between the two excited states is expressed as $\omega_{21} = \omega_2 - \omega_1$. The dynamic Stark shifts are denoted by the Rabi frequencies Ω_1 and Ω_2, as presented in **Figure 10**. The wave function of the total system in the stationary lasers is defined through laser-molecular interactions as

$$\Phi(t) = c_0(t)\exp(-i\omega_0 t)\phi_0 + c_1(t)\exp(-i\omega_1 t)\phi_1 + c_2(t)\exp(-i\omega_2 t)\phi_2. \tag{27}$$

Here, the normalization condition for the coefficients $c_0(t)$, $c_1(t)$, and $c_2(t)$ are as follows,

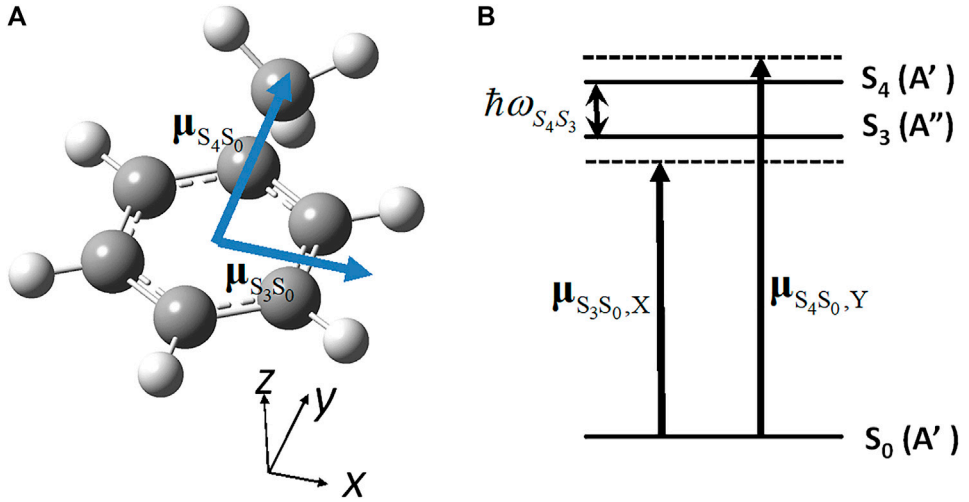

FIGURE 11 | (A) Geometrical structure of toluene molecule (C_S) in the ground state (S_0) with the directions of the two electronic transition dipole moments; **(B)** Parameters for the three electronic states adopted to induce the unidirectional angular momentum: $\hbar\omega_{S_4S_3}$ = 0.10 eV as the energy difference between S_4 and S_3, $\mu_{S_3S_0,X}$ = 5.27 D, and $\mu_{S_4S_0,Y}$ = 5.67 D as the transition dipole moments, E_{S_3} = 8.2 eV and E_{S_4} = 8.3 eVas the vertical transition energies. The angular momentum matrix element between S_3 and S_4, ℓ_{Z,S_3S_4} = 0.672*i*, is perpendicular to the aromatic ring.

$$\left|c_0(t)\right|^2 + \left|c_1(t)\right|^2 + \left|c_2(t)\right|^2 = 1. \tag{28}$$

The system Hamiltonian interacting with the electric fields is given as

$$H(t) = H_0 + V(t), \tag{29}$$

where H_0 satisfies $H_0\phi_i = \varepsilon_i\phi_i$ for i =0, 1, and 2. In **Eq. 29**, the interaction Hamiltonian $V(t)$ between the system and the two electric fields is written as

$$V(t) = -\boldsymbol{\mu}\cdot\mathbf{F}_a\cos(\omega_a t - \zeta_a) - \boldsymbol{\mu}\cdot\mathbf{F}_b\cos(\omega_b t - \zeta_b). \tag{30}$$

Here $\boldsymbol{\mu} = -e\mathbf{r}$ is the electronic dipole moment operator, where $\mathbf{r}$ means the electron coordinate. $\mathbf{F}_\alpha = F_\alpha\mathbf{e}_\alpha$ ($\alpha = a, b$) is the electric field with amplitude F_α and photo-polarization vector $\mathbf{e}_\alpha$, ζ_α is the initial phase, and ω_α is the central frequency. In **Eq. 30**, the two electric fields denoted by a and b induce non-resonant transitions from the ground state to the two excited states. The selective transition conditions are set by the choice of the laser polarization vectors ($\mathbf{e}_a$ and $\mathbf{e}_b$) satisfying $\boldsymbol{\mu}_{02}\perp\mathbf{e}_a$ and $\boldsymbol{\mu}_{01}\perp\mathbf{e}_b$, respectively.

The time-dependent Schrödinger equation can be written as

$$i\hbar\frac{\partial\Phi(t)}{\partial t} = H(t)\Phi(t). \tag{31}$$

The coefficients must satisfy the coupled differential equation

$$i\hbar\frac{\partial}{\partial t}\begin{pmatrix} c_0(t)\\ c_1(t)\\ c_2(t)\end{pmatrix} = \boldsymbol{H}(t)\begin{pmatrix} c_0(t)\\ c_1(t)\\ c_2(t)\end{pmatrix}, \tag{32}$$

where the interaction Hamiltonian,

$$\boldsymbol{H}(t) = \begin{pmatrix} 0 & V_{01}^a(t) & V_{02}^b(t)\\ V_{10}^a(t) & 0 & 0\\ V_{20}^b(t) & 0 & 0\end{pmatrix}, \tag{33}$$

is applied with $V_{01}^a(t) = \langle\phi_0|\boldsymbol{\mu}\cdot\mathbf{F}_a|\phi_1\rangle\cos(\omega_a t - \zeta_a)exp(-i\omega_{10}t)$ and $V_{02}^b(t) = \langle\phi_0|\boldsymbol{\mu}\cdot\mathbf{F}_b|\phi_2\rangle\cos(\omega_b t - \zeta_b)exp(-i\omega_{20}t)$.

Equation 32 can be rewritten in the rotating approximation (RWA) and solved under the following restriction conditions to obtain the analytical solutions for the time-dependent coefficients $\{c_i(t)\}$. For this purpose, we introduce three conditions that can be set experimentally:

$$\text{i. } V \equiv V_{01}^a = V_{02}^b \quad \text{for the transition magnitudes,} \tag{34a}$$

$$\text{ii. } \Delta \equiv \Delta_2 = -\Delta_1 > 0 \quad \text{for detuning frequencies,} \tag{34b}$$

And

$$\text{iii. } \Delta = \Omega - \frac{\omega_{21}}{2} \text{ to induce the degeneracy condition,} \tag{34c}$$

where the transition magnitudes are $V_{01}^a \equiv -\boldsymbol{\mu}_{01}\cdot\mathbf{F}_a/(2\hbar)$, and $V_{02}^b \equiv -\boldsymbol{\mu}_{02}\cdot\mathbf{F}_b/(2\hbar)$.

In **Eq. 34c**, the two dressed states are assumed to have equal energies, i.e., $\Omega \equiv \Omega_1 = \Omega_2 (= \sqrt{\Delta^2 + 2V^2})$, which is called the Rabi frequency [43]. The three conditions lead to a reduction of the input parameters of the two lasers, such that the two amplitudes (F_a and F_b), and two central frequencies (ω_a and ω_b) are reduced to one input parameter. We take $F_a \equiv F$ hereafter. Analytical expressions for time-dependent coefficients $\{c_i(t)\}$ are given in **Appendix C**.

The time-dependent angular momentum defined as an expectation value of an angular momentum operator $\hat{L}_Z = -i\hbar\frac{\partial}{\partial\varphi} = \left(\hbar\hat{l}_Z, \hat{l}_Z = -i\frac{\partial}{\partial\varphi}\right)$, can be expressed,

$$\begin{aligned} L_Z(t) &= \langle\Phi(t)|\hat{L}_Z|\Phi(t)\rangle \\ &= -2\hbar\mathrm{Im}(l_{Z,12})\mathrm{Im}[c_1{*}(t)c_2(t)exp(-i\omega_{21}t)]. \end{aligned} \tag{35}$$

Here, $l_{Z,12} = \langle\phi_1|\hat{l}_Z|\phi_2\rangle = -\langle\phi_2|\hat{l}_Z|\phi_1\rangle = -l_{Z,21}$ and $l_{Z,12} = i\mathrm{Im}l_{Z,12}$.

4.2 Unidirectional π-Electron Rotations in Toluene

We calculate $L_Z(t)$ (derived in the preceding subsection) in a real molecule, toluene. The simplest three-electronic state model is applied for toluene because the quasi-degenerate states S_3 (A") and S_4 (A′) in toluene (C_s) correspond to the doubly degenerate state S_3 (E_{1u}) in benzene (D_{6h}): Note that the S_3 (E_{1u}) state is a dipole-allowed excited state in benzene (D_{6h}), whereas the other two lower excited states, $S_2(B_{1u})$ and $S_1(B_{2u})$, are dipole-forbidden. The geometry optimization of toluene was carried out with the MP2 level of theory [43]. The C_S symmetry of toluene indicates that one of the hydrogen atoms belonging to the methyl group is perpendicular to an aromatic ring plane (**Figure 11A**).

Figure 12A shows the calculated time-dependent angular momentum expectation values $L_Z(t)$ with respect to the relative phase $\zeta = -\pi/2$ ($\zeta = +\pi/2$) between the two lasers for the left (right) panel. These were calculated using **Eq. 35** combined with **Eq. 34**. Here, the amplitude of the electric field F_a is adopted as the input parameter F ($\equiv F_a$). Other parameters are shown in **Table 3A**, while **Table 3B** shows the time-dependent populations in the three electronic states.

The time-dependent angular momenta plotted in **Figure 12A** are comprised of angular momentum pulse trains of the same shape for each value of F. Each angular momentum pulse corresponds to the unidirectional π-electron rotation, which begins with acceleration and ends with deceleration. The direction of the π-electron rotations is determined by the relative phase ζ between the two lasers: clockwise rotation for $\zeta=+\pi/2$, and anti-clockwise rotation for $\zeta=-\pi/2$. Here we discuss how the unidirectional π-electron rotations are created. We first note that $L_Z(t)$ can be rewritten under the two conditions, **Eq. 34a** and **Eq. 34b**, for $\Omega\approx\Delta$ as

$$L_Z(t) \approx 4\hbar \mathrm{Im}\left(l_{Z,12}\right)\frac{V^2\Delta^2}{\Omega^4}\left(1-\cos\Omega t\right)\sin\left((2\Delta+\omega_{21}-\Omega)t+\zeta\right). \tag{36}$$

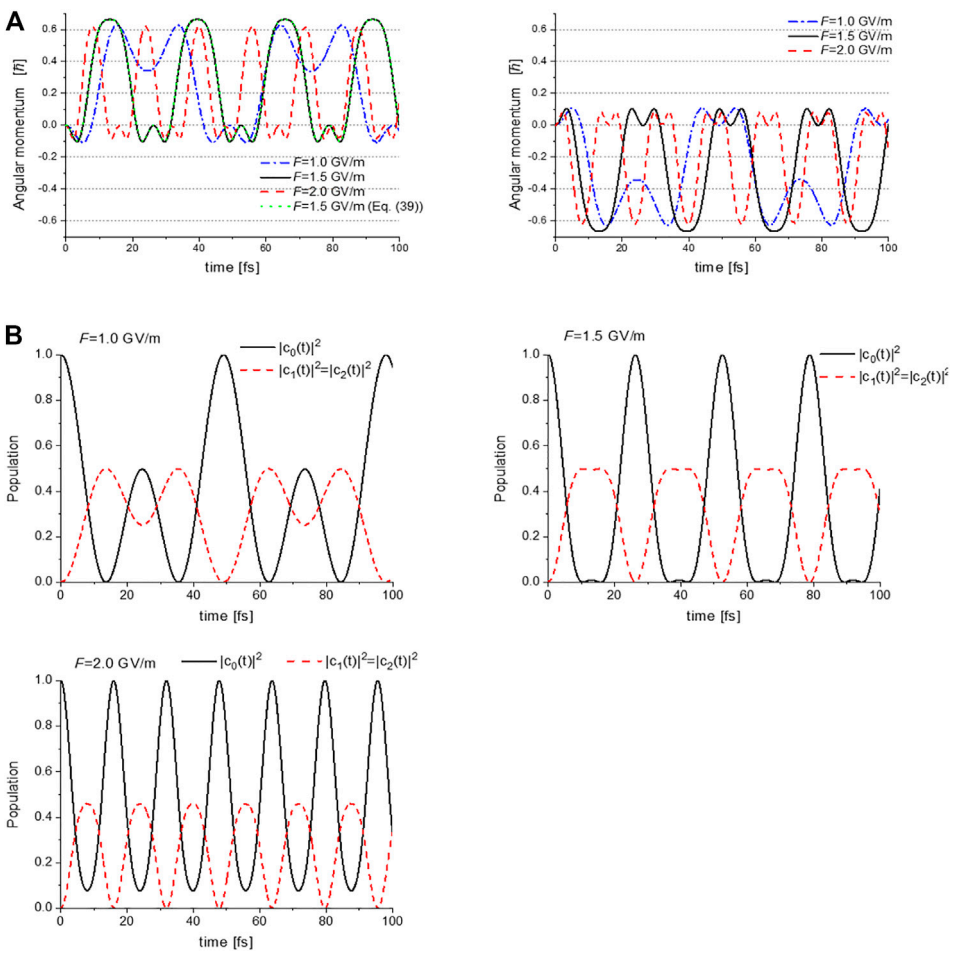

FIGURE 12 | (A) Expectation values of the angular momentum operator $L_Z(t)$ for toluene, calculated with the laser input parameter values F = 1.0, 1.5 and 2.0 GV/m. The left **(right)** panel shows $L_Z(t)$ with respect to the relative phase between two lasers $\zeta = -\pi/2$ ($\zeta = +\pi/2$); **(B)** Temporal evolutions of the populations in S_0, S_3, and S_4 for F = 1.0, 1.5 and 2.0 GV/m. Reprinted with permission from Ref. [43] Copyright (2016) Royal Society of Chemistry.

TABLE 3A | Input parameter F ($\equiv F_a$) and other parameters for a generation of unidirectional π-electron rotation in toluene.

F [GV/m] ([W/cm^2])	2|V| [eV]	Ω [eV]	|V|/Ω	Δ [eV]	ω_a [eV]	ω_b [eV]
1.0 (0.13×10^{12})	0.110	0.084	0.655	0.032	8.16	8.33
1.5 (0.30×10^{12})	0.165	0.157	0.525	0.105	8.09	8.40
2.0 (0.53×10^{12})	0.220	0.260	0.423	0.208	7.99	8.51

Reprinted with permission from Ref. [43] Copyright (2016) Royal Society of Chemistry.

Table 3B | Calculated physical properties of the unidirectional π-electron rotation in toluene.

F [GV/m]	T [fs][a]	τ [fs][a]	$\bar{L}_Z[\hbar]$[a]	J [μA]	N_r
1.0	49.2	12.6	0.084	16.8	3.90
1.5	26.3	6.40	0.166	33.2	4.10
2.0	15.9	6.87	0.155	31.0	2.32

[a]*Parameters V, Δ, Ω, ω_a, and ω_b, were calculated for three values of F using* ***Eq. 34****. These parameters used for the calculation of the following physical quantities: T as a period of Rabi oscillation; $\bar{L}_Z$ is the angular momentum averaged over one cycle period of Rabi oscillation, $\tau = 2\pi m_e r/p = 2\pi m_e r^2/|\bar{L}_Z|$ as the rotational period of a π-electron, J as a ring current, and $N_r \equiv T/\tau$ as one cycle count of π-electron rotations.*

Equation 36 expresses no unidirectional π-electron rotations. By introducing the third condition, **Eq. 34c**, which provides for the formation of the doubly degenerate dressed states with $\zeta = \pm\pi/2$, **Eq. 36** can be expressed as

$$L_Z(t) \approx 4\hbar \mathrm{Im}(l_{Z,12}) \frac{V^2\Delta^2}{\Omega^4}(1-\cos\Omega t)\sin(\Omega t+\zeta). \qquad (37)$$

This indicates a unidirectional π-electron rotation whose direction is determined by the relative phase ζ, that is, $L_Z(t) > 0$ for $\zeta = -\pi/2$ and $L_Z(t) < 0$ for $\zeta = +\pi/2$, as demonstrated in **Figure 12**. The dotted line shown in **Figure 12A** represents $L_Z(t)$ for $F = 1.5$ GV/m as calculated by **Eq. 37**, which well reproduces $L_Z(t)$ curve calculated using **Eq. 35** without the approximation of $\Omega \approx \Delta$ approximation. Thus, the unidirectional π-electron rotation originates from the DSIDES formed by the two non-resonant lasers with a definite relative phase of $\pm\pi/2$.

As demonstrated in **Figure 12A**, the oscillation periods of the angular momentum pulses become shorter (higher Rabi frequency Ω), and those amplitudes decrease as F increases. These two behaviors result from the third restriction condition for degeneracy (**Eq. 35c**) used in the derivation of $L_Z(t)$. This degeneracy condition should be satisfied for the two dressed states with equal energies to maintain their energies located at the center of the two excited states, even though the laser intensities of two lasers increase. This results in an increase in the detuning parameter Δ of the two lasers, that is, a decrease (increase) in ω_a (ω_b), as shown in **Table 3A**.

Figure 12A exhibits that the maximum magnitude of the angular momentum occurs in the vicinity of $F = 1.5$ GV/m. This can be explained by noting that the constant in **Eq. 37**, $V^2\Delta^2/\Omega^4$, with Rabi frequency of $\Omega = \sqrt{\Delta^2 + 2V^2}$, reaches its maximum at $\Delta^2 = 2V^2$, which in turn provides the maximum angular momentum. Using the relationship $\Delta^2 = 2V^2$for the dressed states with equal energies in **Eq. 34c**, the electric field F is estimated as $F = \sqrt{2}\hbar\Delta/(\boldsymbol{\mu}_{10})_X = 1.52$ GV/m with $\Delta = 0.118$ eV, which is close to the $F = 1.5$ GV/m value shown in **Figure 12A**.

Figure 12B shows the F-dependence of the $|c_{S_0}(t)|^2$, $|c_{S_3}(t)|^2$ and $|c_{S_4}(t)|^2$ populations in toluene, which were calculated using Eqs. (B2). The relationship between the excited state populations, $|c_{S_3}(t)|^2 = |c_{S_4}(t)|^2$, is maintained because the conditions represented by **Eqs. 34a**, **34b**, were used for a derivation of $L_Z(t)$. Inversion of populations between the ground and excited states occurs for $F = 1.5$ GV/m and 2.0 GV/m, as demonstrated in **Figure 12B**. By comparing **Figures 12A,B**, it can be observed that major components of the unidirectional angular momentum pulse are created during when the population inversion occurs.

We now estimate the physical constants associated with π-electron rotations, which are listed in **Table 3B**: one cycle count of π-electron rotation N_r, and the magnitude of ring current J in one cycle of Rabi oscillation with periodicity $T \equiv 2\pi/\Omega$. In particular for aromatic molecules the ring current is an important physical quantity because it is directly related to the magnetic field induced by the ring current. For simplicity, we consider the classical model of π-electron rotation, in which N_r is defined as $N_r \equiv T/\tau$. Here $\tau = 2\pi m_e r/p = 2\pi m_e r^2/|\bar{L}_Z|$ is the rotational period of a π-electron having an angular momentum averaged over one cycle period of Rabi oscillation ($\bar{L}_Z$). m_e is the electron mass, and r indicates the radius of the aromatic ring. $\bar{L}$ was calculated using **Eq. 37** substituting for $L_Z(t)$ as

$$\bar{L}_Z = \frac{1}{T}\int_0^T dt L_Z(t) = -\frac{2\hbar \mathrm{Im} l_{Z,12}}{\Omega^4} V^2\Delta^2 \sin\zeta. \qquad (38)$$

The ring current can be approximately expressed as $J \approx \bar{L}_Z J_0/\hbar$ [39–41, 43]. Here on a single aromatic ring, $J_0 = 200$ μA was a typical value of the ring current estimated with a unit angular momentum $\hbar$. **Table 3B** exhibits the calculated ring current J, cycle counts of π-electron rotations along the aromatic ring N_r and three values of F adopted in **Figure 12**, together with the parameters used in this model calculation. In **section 3**, we presented a pump-dump control procedure for the generation of sequential unidirectional ring currents in a 2,2'-biphenol

molecule having non-degenerate excited states. The same order of magnitudes of the pump- and dump- pulse lasers were applied in the vicinity of ~1 GV/m, considering that the number of aromatic rings differs between biphenol and toluene. This can be explained by the point that the magnitudes of the ring current J or the angular momentum $\overline{L}_Z$ are proportional to that of the coherence between the two excited states, but not proportional to the number of aromatic rings. It is remarkable that in **Table 3B** J is not proportional to N_r, it is actually proportional to N_r/T. This is originated from the different behaviors between J and N_r related to the F-dependence shown in **Table 3B**.

5 SUMMARY AND PERSPECTIVE

This paper briefly provides an overview of the theoretical study of quantum laser control of coherent π-electron dynamics in low-symmetry aromatic ring molecules, which we have undertaken in recent several years [39–43, 68–73]. The essential principles to generate the π-electron angular momentum and ring current in a low symmetry aromatic ring molecule are first to create a superposition of two electronic excited (coherent) states using two linearly polarized lasers, and second to select the clockwise or anticlockwise rotational component from the non-stationary time evolution of the coherent state using pump and dump lasers with properly designed polarization directions. Here, the direct product of the irreducible representations of each excited states in the molecular point group belongs to that of the molecular rotation, (Rx, Ry or Rz), and the relative phase between the two linearly polarized lasers are fixed in order to determine the initial direction of the angular momentum and ring current. In additon to the laser conditions, aromatic ring molecules also need to satisfy the follwing conditions to generate the π-electron angular momentum and ring current. First two electronic excited states are nearly degenerate, and second, those states can be excited from the ground states using UV lasers, i.e., transitions between the electronic excited states and ground states are optically allowed.

On the basis of the above principles, analytical expressions for coherent π-electron angular momentum, ring current, and ring current-induced magnetic field are derived in the quantum chemical MO theory. A coherent π-electron ring current is defined as the average of the bond currents. Temporal behaviors of these coherent quantities are calculated using the density matrix method within the Markov approximation. Quantum simulations of the coherent quantuities have been performed for (*P*)-2,2'-biphenol. Based on the simulation results a new quantum control method for two-dimensional ultrafast angular momentum switching was proposed. The essential point of the quantum control is to use a sequence of the overlapped pump and dump pulses with a selected relative phase and selected polarization directions between the two lasers. The results for the (*P*)-2,2'-biphenol indicate that this new control scheme can potentially be used for the design and realization of ultrafast multi-dimensional electronic switching devices, or field-effect transistor devices.

The familiar quantum optimal control procedure was applied to an optiaml control of the coherent π-electron ring currents in planar PAHs with D_{2h} symmetry. For this purpose, we have to set up the target state for a desired ring current pattern. The final target wave functions are determined *via* the Lagrange multiplier method by solving the coupled equations of motion under the constraints that the ring currents must satisfy. The method was applied to anthracene. The creation of the perimeter current and the middle ring current in anthracene were successfully realized. The control mechanisms were elucidated by analyzing the time-dependent behaviors of the control laser puses and the populations of the relevant electronic states. Concerning the types of molecules used in the above laser control studies, polycyclic planar aromatic molecules like PAHs, coronene and benzoic acids dimers are applicable for a laser control of perimeter or localized ring currents.

Another laser control method for the π-electrons unidirectional rotation in low symmetric aromatic rings was presented. The basic idea of the control method is to degenerate two nondegenerate excited states by using dynamic Stark shifts. Doubly degenerate excited state was created by the Stark shift using the two linearly polarized non-resonant lasers with a definite relative phase of $\pm\frac{\pi}{2}$, which determines the angular momentum direction (clockwise or anti-clockwise π-electron rotation). Applying the RWA, the coherent π-electron angular momentum in a three-electronic state model was analytically expressed in a closed form, and the proposed control theory have been applied to toluene (Cs). The numerical simulations indicated that the resulting angular momentum comprised sequential angular momentum pulses with a positive or negative value depending on the relative phases between the two lasers.

Some theoretical studies on laser control of the coherent π-electron rotations that were not included in this review are noteworthy. Probing molecular chirality, right-handed or left-handed chiral molecules, is a central issue in natural science. E.x., Phenylalanine is an essential amino acid, and L-enantiomer is found in natural system. On the other hand, D-enantiomer is synthesized artificially, and racemate phenylalanine is used for dietary supplement. However, in conventional methods such as CD spectroscopy and optical rotatory dispersion (ORD) spectroscopy [74, 75], the signals are very week because these processes involve second-order evaluations. As a possible of laser control scheme of the unidirectional π-electron rotations in low symmetric aromatic ring molecules, we previously proposed an efficient enantiomer-probing scenario for chiral aromatic molecule [71, 72]. A pair of nondegenerate excited states becomes degenerate by applying the dynamic Stark shift in the presence of two non-resonant UV lasers, producing an enantiomer-specific angular momentum. In that study, phenylalanine was adopted as an example for the numerical simulation. The resulting enantiomer-specific magnetic fluxes were on the order of a few Tesla, with periods of several tens of femtoseconds.

The contribution of vibrational motion to coherent π-electron rotations is also an important research topic that was not discussed in this review. In our previous research, vibrational

effects on the coherent π-electron rotations in (*P*)-2,2'-biphenol were theoretically studied in the adiabatic approximation [73]. It was found that the low-frequency torsion mode around the bridge causes modulations in the beat of the ring current [73]. The vibrational effects on dynamic Stark-induced π-electron rotations in aromatic ring molecules with low symmetry were also studied using the displaced harmonic oscillator (DHO) model in the adiabatic approximation [72]. A pair of the lowest vibronic state in the two electronic excited states was degenerated using the two linearly polarized UV lasers. The two potential displacements between the ground state and the two electronic excited states were used as the parameters. The shapes of the sequential angular momentum pulses were affected by the potential displacements.

From one perspective, theoretical treatments beyond the adiabatic approximation [28, 31, 74–77] are expected to be incorporated such that other electronic excited states interact with the two relevant excited states through nonadiabatic couplings. It is crucial to clarify the effect of nonadiabatic couplings to the unidirectional π-electron rotations and determine how to maintain π-electron rotations by way of quantum optimal control techniques. In large PAHs, once π-electron rotation is realized at a localized ring site and once a site-selective coherent ring current is generated, the localized ring current is transferred from site to site using the laser pulses, i.e., transferred ring currents, which allow for an ultrafast switching function at the selected local site. Furthermore, the site-selective coherent ring current and transferred ring current can create the induced magnetic fields. These electromagnetic fields are expected to provide ultrafast probing of local sites in large molecular systems, biomolecules with chiral aromatic ring molecules, and PAHs. Further development of theoretical treatments involving photon-induced electronic coherence in molecular systems would be promising in the near future.

AUTHOR CONTRIBUTIONS

The authors made a substantial, direct, and intellectual contribution to the work and approved it for publication. Original draft preparation, software, formal analysis, and funding acquisition, HM; Conceptualization, supervision, project administration, and validation, YF; Writing—original draft preparation, HM and YF; Investigation, writing—review and editing, HM, N-LP, and YF.

ACKNOWLEDGMENTS

HM and YF are grateful to Dr. M. Yamaki, and Professors Y. Teranishi, G-S. Kim, Y.J. Yan, and H. Nakamura for their contribution in earlier works. YF would like to thank Professor S. H. Lin for his critical comments and financial support.

REFERENCES

1. Goulielmakis E, Loh Z-H, Wirth A, Santra R, Rohringer N, Yakovlev VS, et al. Real-time Observation of Valence Electron Motion. *Nature* (2010) 466: 739–43. doi:10.1038/nature09212
2. Yuan K-J, and Bandrauk AD Circularly Polarized Attosecond Pulses from Molecular High-Order Harmonic Generation by Ultrashort Intense Bichromatic Circularly and Linearly Polarized Laser Pulses. *J Phys B: Mol Opt Phys* (2012) 45:074001. doi:10.1088/0953-4075/45/7/074001
3. Chen S, Gilbertson S, Wang H, Chini M, Zhao K, Khan SD, et al. Attosecond Pulse Generation, Characterization and Application. *Adv Multiphoton Process. Spectrosc* (2011) 20:127–74. doi:10.1142/9789814343992_0004
4. Remacle F, and Levine RD Attosecond Pumping of Nonstationary Electronic States of LiH: Charge Shake-Up and Electron Density Distortion. *Phys Rev A* (2011) 83:013411. doi:10.1103/PhysRevA.83.013411
5. Tzallas P, Skantzakis E, Kruse JE, and Charalambidis D On the Generation of Intense Isolated Attosecond Pulses by Many-Cycle Laser Fields. In: *Progress in Ultrafast Intense Laser Science*. Heidelberg: Springer (2011). p. 163–90. doi:10.1007/978-3-642-18327-0_8
6. Ulusoy IS, and Nest M Correlated Electron Dynamics: How Aromaticity Can Be Controlled. *J Am Chem Soc* (2011) 133:20230–6. doi:10.1021/ja206193t
7. Fujimura Y, and Sakai H *Electronic and Nuclear Dynamics in Molecular Systems*. Singapore: World Scientific (2011). p. 117–32.
8. Singh KP, He F, Ranitovic P, Cao W, De S, Ray D, et al. Control of Electron Localization in Deuterium Molecular Ions Using an Attosecond Pulse Train and a Many-Cycle Infrared Pulse. *Phys Rev Lett* (2010) 104:023001. doi:10.1103/PhysRevLett.104.023001
9. Krausz F, and Ivanov M Attosecond Physics. *Rev Mod Phys* (2009) 81:163–234. doi:10.1103/RevModPhys.81.163
10. Nest M, Remacle F, and Levine RD Pump and Probe Ultrafast Electron Dynamics in LiH: A Computational Study. *New J Phys* (2008) 10:025019. doi:10.1088/1367-2630/10/2/025019
11. Kling MF, and Vrakking MJJ Attosecond Electron Dynamics. *Annu Rev Phys Chem* (2008) 59:463–92. doi:10.1146/annurev.physchem.59.032607.093532
12. Skourtis SS, Beratan DN, Naaman R, Nitzan A, and Waldeck DH Chiral Control of Electron Transmission through Molecules. *Phys Rev Lett* (2008) 101:238103. doi:10.1103/PhysRevLett.101.238103
13. NabekawaMidorikawa YK, and Midorikawa K Nonlinear Optics for Characterizing XUV/Soft X-ray High-Order Harmonic Fields in Attosecond Regime. *Adv Multiphoton Process. Spectrosc* (2008) 18:1–67. doi:10.1142/9789812791740_0001
14. Lein M, and Chirilă CC Signatures of Molecular Structure and Dynamics in High-Order Harmonic Generation. *Adv Multiphoton Process. Spectrosc* (2008) 18:69–106. doi:10.1142/9789812791740_0002
15. Corkum PB, and Krausz F Attosecond Science. *Nat Phys* (2007) 3:381–7. doi:10.1038/nphys620
16. Remacle F, Nest M, and Levine RD Laser Steered Ultrafast Quantum Dynamics of Electrons in LiH. *Phys Rev Lett* (2007) 99:183902. doi:10.1103/PhysRevLett.99.183902
17. Räsänen E, Castro A, Werschnik J, Rubio A, and Gross EKU Optimal Control of Quantum Rings by Terahertz Laser Pulses. *Phys Rev Lett* (2007) 98:157404. doi:10.1103/PhysRevLett.98.157404
18. Klamroth T Optimal Control of Ultrafast Laser Driven many-electron Dynamics in a Polyatomic Molecule: N-Methyl-6-Quinolone. *J Chem Phys* (2006) 124:144310. doi:10.1063/1.2185633
19. Pershin YV, and Piermarocchi C Laser-controlled Local Magnetic Field with Semiconductor Quantum Rings. *Phys Rev B* (2005) 72:245331. doi:10.1103/PhysRevB.72.245331
20. Niikura H, Légaré F, Hasbani R, Ivanov MY, Villeneuve DM, and Corkum PB Probing Molecular Dynamics with Attosecond Resolution Using Correlated Wave Packet Pairs. *Corkum PBNature* (2003) 421:826–9. doi:10.1038/nature01430
21. Haruyama K, kono H, Fujimura Y, Kawata I, and Bandrauk AD Intense Laser-Field Ionization of H2 Enhanced by Two-Electron Dynamics. *Phys Rev A* (2002) 66:043403. doi:10.1103/PhysRevA.66.043403

22. Anthony JE Functionalized Acenes and Heteroacenes for Organic Electronics. *Chem Rev* (2006) 106:5028–48. doi:10.1021/cr050966z
23. Bonifas AP, and McCreery RL 'Soft' Au, Pt and Cu Contacts for Molecular Junctions through Surface-Diffusion-Mediated Deposition. *Nat Nanotech* (2010) 5:612–7. doi:10.1038/nnano.2010.115
24. BarthManz IJ, and Manz J Periodic Electron Circulation Induced by Circularly Polarized Laser Pulses: Quantum Model Simulations for Mg Porphyrin. *Angew Chem Int Ed* (2006) 45:2962–5. doi:10.1002/anie.200504147
25. Barth I, Manz J, Shigeta Y, and Yagi K Unidirectional Electronic Ring Current Driven by a Few Cycle Circularly Polarized Laser Pulse: Quantum Model Simulations for Mg−Porphyrin. *J Am Chem Soc* (2006) 128:7043–9. doi:10.1021/ja057197l
26. Barth I, and Manz J Quantum Switching of Magnetic Fields by Circularly Polarized Re-optimized π Laser Pulses: From One-Electron Atomic Ions to Molecules. In: *Progress in Ultrafast Intense Laser Science VI*. Berlin, Heidelberg: Springer (2010). p. 21–44. doi:10.1007/978-3-642-15054-8_2
27. Nobusada K, and Yabana K Photoinduced Electric Currents in Ring-Shaped Molecules by Circularly Polarized Laser Pulses. *Phys Rev A* (2007) 75:032518. doi:10.1103/PhysRevA.75.032518
28. Kanno M, Kono H, and Fujimura Y Control of π-Electron Rotation in Chiral Aromatic Molecules by Nonhelical Laser Pulses. *Angew Chem Int Ed* (2006) 45: 7995–8. doi:10.1002/anie.200602479
29. Kanno M, Hoki K, Kono H, and Fujimura Y Quantum Optimal Control of Electron Ring Currents in Chiral Aromatic Molecules. *J Chem Phys* (2007) 127: 204314. doi:10.1063/1.2806180
30. Kanno M, Kono H, Fujimura Y, and Lin SH Nonadiabatic Response Model of Laser-Induced Ultrafastπ-Electron Rotations in Chiral Aromatic Molecules. *Phys Rev Lett* (2010) 104:108302. doi:10.1103/PhysRevLett.104.108302
31. Kanno M, Kono H, and Fujimura Y Control of π-Electron Rotations in Chiral Aromatic Molecules Using Intense Laser Pulses. In: *Progress in Ultrafast Intense Laser Science VII*. Berlin, Heidelberg: Springer (2011). p. 53–78. doi:10.1007/978-3-642-18327-0_3
32. Barth I, Manz J, and Serrano-Andrés L Quantum Simulations of Toroidal Electric Ring Currents and Magnetic fields in Linear Molecules Induced by Circularly Polarized Laser Pulses. *Chem Phys* (2008) 347:263–71. doi:10.1016/j.chemphys.2007.09.037
33. Yuan K-J, and Bandrauk AD Attosecond-magnetic-field-pulse Generation by Coherent Circular Molecular Electron Wave Packets. *Phys Rev A* (2015) 91: 042509. doi:10.1103/PhysRevA.91.042509
34. Steiner E, and Fowler PW Patterns of Ring Currents in Conjugated Molecules: A Few-Electron Model Based on Orbital Contributions. *J Phys Chem A* (2001) 105:9553–62. doi:10.1021/jp011955m
35. Lazzerretti P Ring Currents. *Prog Nucl Magn Reson Spectrosc* (2000) 36:1–88. doi:10.1016/S0079-6565(99)00021-7
36. Redfield AG The Theory of Relaxation Processes. *Adv Magn Reson* (1965) 1: 1–32. doi:10.1016/B978-1-4832-3114-3.50007-6
37. Lindblad G On the Generators of Quantum Dynamical Semigroups. *Commun.Math Phys* (1976) 48:119–30. doi:10.1007/BF01608499
38. Lin SH, Chang CH, Liang KK, Chang R, Shiu YJ, Zhang JM, et al. Ultrafast Dynamics and Spectroscopy of Bacterial Photosynthetic Reaction Centers. *Adv Chem Phys* (2002) 12:1–88. doi:10.1002/0471264318.ch1
39. Mineo H, Lin SH, and Fujimura Y Coherent π-electron Dynamics of (P)-2,2′-biphenol Induced by Ultrashort Linearly Polarized UV Pulses: Angular Momentum and Ring Current. *J Chem Phys* (2013) 138:074304. doi:10.1063/1.4790595
40. Mineo H, Yamaki M, Teranishi Y, Hayashi M, Lin SH, and Fujimura Y Quantum Switching of π-Electron Rotations in a Nonplanar Chiral Molecule by Using Linearly Polarized UV Laser Pulses. *J Am Chem Soc* (2012) 134: 14279–82. doi:10.1021/ja3047848
41. Mineo H, and Fujimura Y Quantum Design of π-Electron Ring Currents in Polycyclic Aromatic Hydrocarbons: Parallel and Antiparallel Ring Currents in Naphthalene. *J Phys Chem Lett* (2017) 8:2019–25. doi:10.1021/acs.jpclett.7b00704
42. Mineo H, and Fujimura Y Quantum Control of Coherent π-electron Ring Currents in Polycyclic Aromatic Hydrocarbons. *J Chem Phys* (2017) 147: 224301. doi:10.1063/1.5004504
43. Mineo H, Yamaki M, Kim G-S, Teranishi Y, Lin SH, and Fujimura Y Induction of Unidirectional π-electron Rotations in Low-Symmetry Aromatic Ring Molecules Using Two Linearly Polarized Stationary Lasers. *Phys Chem Chem Phys* (2016) 18:26786–95. doi:10.1039/C6CP04254F
44. Oda K, Hita M, Minemoto S, and Sakai H All-Optical Molecular Orientation. *Phys Rev Lett* (2010) 104:213901. doi:10.1103/PhysRevLett.104.213901
45. Stapelfeldt H, and Seideman T Colloquium: Aligning Molecules With strong Laser Pulses. *Rev Mod Phys* (2003) 75:543–57. doi:10.1103/RevModPhys.75.543
46. Kanai T, Minemoto S, and Sakai H Quantum Interference during High-Order Harmonic Generation From Aligned Molecules. *Nature* (2005) 435:470–4. doi:10.1038/nature03577
47. Frisch MJ, Trucks GW, Schlegel HB, Scuseria GE, Robb MA, Cheeseman JR, et al. *Gaussian 09, Revision E.01*. Wallingford, CT: Gaussian, Inc. (2009).
48. Baskin JS, Felker PM, and Zewail AH Doppler-free Time-resolved Polarization Spectroscopy of Large Molecules: Measurement of Excited State Rotational Constants. *J Chem Phys* (1986) 84:4708–10. doi:10.1063/1.449998
49. Mineo H, Lin SH, Fujimura Y, Xu J, Xu RX, and Yan YJ Non-Markovian Response of Ultrafast Coherent Electronic Ring Currents in Chiral Aromatic Molecules in a Condensed Phase. *J Chem Phys* (2013) 139:214306. doi:10.1063/1.4834035
50. Barth I, and Manz J Electric Ring Currents in Atomic Orbitals and Magnetic Fields Induced by Short Intense Circularly Polarizedπlaser Pulses. *Phys Rev A* (2007) 75:012510. doi:10.1103/PhysRevA.75.012510
51. Barth I, Serrano-Andrés L, and Seideman T Nonadiabatic Orientation, Toroidal Current, and Induced Magnetic Field in BeO Molecules. *J Chem Phys* (2008) 129:164303. doi:10.1063/1.2994737
52. Acremann Y, Buess M, Back CH, Dumm M, Bayreuther G, and Pescia D A Single Ion as a Nanoscopic Probe of an Optical Field. *Nature* (2001) 414:49–51. doi:10.1038/35102129
53. Kruglyak VV, Portnoi ME, and Hicken RJ Use of the Faraday Optical Transformer for Ultrafast Magnetization Reversal of Nanomagnets. *J Nanophoton* (2007) 1:013502. doi:10.1117/1.2516174
54. Kirilyuk A, Kimel AV, and Rasing T Ultrafast Optical Manipulation of Magnetic Order. *Rev Mod Phys* (2010) 82:2731–84. doi:10.1103/RevModPhys.82.2731
55. Kanno M, Ono Y, Kono H, and Fujimura Y Laser-Polarization Effects on Coherent Vibronic Excitation of Molecules with Quasi-Degenerate Electronic States. *J Phys Chem A* (2012) 116:11260–72. doi:10.1021/jp305284w
56. Bandrauk AD, Fujimura Y, and Gordon RJ *Laser Control and Manipulation of Molecules*. Washington, DC: American Chemical Society (2002). p. 821. doi:10.1021/bk-2002-0821.fw001
57. Gordon R, Zhu LC, and Seideman T Coherent Control of Chemical Reactions. *Acc Chem Res* (1999) 12:1007–16. doi:10.1021/ar970119l
58. Krause P, Klamroth T, and Saalfrank P Time-dependent Configuration-Interaction Calculations of Laser-Pulse-Driven Many-electron Dynamics: Controlled Dipole Switching in Lithium Cyanide. *J Chem Phys* (2005) 123: 074105. doi:10.1063/1.1999636
59. Zhu W, Botina J, and Rabitz H Rapidly Convergent Iteration Methods for Quantum Optimal Control of Population. *J Chem Phys* (1998) 108:1953–63. doi:10.1063/1.475576
60. Zhu W, and Rabitz H A Rapid Monotonically Convergent Iteration Algorithm for Quantum Optimal Control over the Expectation Value of a Positive Definite Operator. *J Chem Phys* (1998) 109:385–91. doi:10.1063/1.476575
61. Ohtsuki Y, Zhu W, and Rabitz H Monotonically Convergent Algorithm for Quantum Optimal Control with Dissipation. *J Chem Phys* (1999) 110:9825–32. doi:10.1063/1.478036
62. Ferguson J, Reeves LW, and Schneider WG VAPOR ABSORPTION SPECTRA AND OSCILLATOR STRENGTHS OF NAPHTHALENE, ANTHRACENE, AND PYRENE. *Can J Chem* (1957) 35:1117–36. doi:10.1139/v57-152
63. Rodriguez JJ, and Mukamel S Probing Ring Currents in Mg-Porphyrins by Pump-Probe Spectroscopy. *J Phys Chem A* (2012) 116:11095–100. doi:10.1021/jp3035874
64. Yuan K-J, Shu C-C, Dong D, and Bandrauk AD Attosecond Dynamics of Molecular Electronic Ring Currents. *J Phys Chem Lett* (2017) 8:2229–35. doi:10.1021/acs.jpclett.7b00877
65. Rugar D, Budakian R, Mamin HJ, and Chui BW Single Spin Detection by Magnetic Resonance Force Microscopy. *Nature* (2004) 430:329–32. doi:10.1038/nature02658
66. Repp J, Meyer G, Stojković SM, Gourdon A, and Joachim C Molecules on Insulating Films: Scanning-Tunneling Microscopy Imaging of Individual

Molecular Orbitals. *Phys Rev Lett* (2005) 94:026803. doi:10.1103/PhysRevLett.94.026803
67. Sloan PA Time-resolved Scanning Tunnelling Microscopy for Molecular Science. *J Phys Condens Matter* (2010) 22:264001. doi:10.1088/0953-8984/22/26/264001
68. Yamaki M, Teranishi Y, Nakamura H, Lin SH, and Fujimura Y The Generation of Stationary π-electron Rotations in Chiral Aromatic Ring Molecules Possessing Non-degenerate Excited States. *Phys Chem Chem Phys* (2016) 18:1570–7. doi:10.1039/C5CP05467B
69. Mineo H, Lin SH, and Fujimura Y Vibrational Effects on UV/Vis Laser-Driven π-electron Ring Currents in Aromatic Ring Molecules. *Chem Phys* (2014) 442:103–10. doi:10.1016/j.chemphys.2014.02.011
70. Mineo H, Phan N-L, La D-K, and Fujimura Y Theoretical Study of Dynamic Stark-Induced π-Electron Rotations in Low-Symmetry Aromatic Ring Molecules Beyond the Frozen Nuclear Approximation. *J Phys Chem A* (2021) 125:1476–89. doi:10.1021/acs.jpca.0c10216
71. Mineo H, Kim G-S, Lin SH, and Fujimura Y Dynamic Stark-Induced Coherent π-Electron Rotations in a Chiral Aromatic Ring Molecule: Application to Phenylalanine. *J Phys Chem A* (2019) 123:6399–410. doi:10.1021/acs.jpca.9b03083
72. Mineo H, Kim G-S, Lin SH, and Fujimura Y Quantum Design for Ultrafast Probing of Molecular Chirality through Enantiomer-specific Coherent π-Electron Angular Momentum. *J Phys Chem Lett* (2018) 9:5521–6. doi:10.1021/acs.jpclett.8b02137
73. Mineo H, Kanno M, Kono H, Chao SD, Lin SH, and Fujimura Y Ultrafast Coherent Dynamics of Nonadiabatically Coupled Quasi-Degenerate Excited States in Molecules: Population and Vibrational Coherence Transfers. *Chem Phys* (2012) 392:136–42. doi:10.1016/j.chemphys.2011.11.004
74. Barron LD *Molecular Light Scattering and Optical Activity*. Cambridge, UK: Cambridge University Press (1982).
75. JM Hicks, eds. *Chirality: Physical Chemistry*. Washington, DC; American Chemical Society, (2002) 1–16.
76. Nakamura H *Nonadiabatic Transition Concept, Basic Theories and Applications, Chapter 10. Multi-Dimensional Problems*. Singapore: World Scientific (2012) 212–44.
77. de Vivie-Riedle R, and Hofmann A Nonadiabatic Quantum Dynamics and Control Strategies. In: W Domcke, DR Yarkony, and H Köppel, eds. *Conical Intersections, Electronic Structure, Dynamics & Spectroscopy*. New Jersey: World Scientific, (2004) 803–27.

Conflict of Interest: The authors declare that the research was conducted in the absence of any commercial or financial relationships that could be construed as a potential conflict of interest.

APPENDIX

A BRIEF DERIVATION OF TARGET OPERATORS, CALCULATED USING THE COUPLED EQUATIONS FOR THE RING CURRENT LOCALIZATION (EQ. 19).

In general, the Lagrange function L_J consists of "the function to be maximized or minimized" and "all related constraint conditions of the system," For the localization of the π-electron ring current, J_χ in PAHs, $L_J(c_1,\cdots,c_n,\lambda_1,\cdots,\lambda_m)$ can be rewritten as

$$L_J(c_1,\cdots,c_n,\lambda_1,\cdots,\lambda_m) = J_\chi + \lambda_1 J_1 + \cdots + \lambda_{\chi-1}J_{\chi-1} + \lambda_\chi\left(\sum_{\alpha=1}^{n}|c_\alpha|^2 - 1\right) + \lambda_{\chi+1}J_{\chi+1} + \cdots + \lambda_m J_m, \quad \text{(A1)}$$

Where the first term J_χ is the target ring current to be maximized, while the other terms with Lagrange multiplier λ_κ, $J_\kappa \equiv J_\kappa(T)$, are irrelevant to the localization under the constraint conditions, such that $J_1 = \cdots = J_{\chi-1} = J_{\chi+1} = \cdots = J_m = 0$, and $(\sum_{\alpha=1}^{n}|c_\alpha|^2 - 1) = 0$, which indicates the number conservation of the π-electrons associated with the ring current.

The partial derivatives of **Eq. 19** with respect to $x_\alpha = (\mathrm{Re}c_\alpha, \mathrm{Im}c_\alpha)$, λ_χ and λ_κ are then

$$\frac{\partial L_J}{\partial x_\alpha} = \frac{\partial J_\chi}{\partial x_\alpha} + \sum_{\kappa\neq\chi}^{m}\lambda_\kappa\frac{\partial J_\kappa}{\partial x_\alpha} + \lambda_\chi\frac{\partial}{\partial x_\alpha}\left(\sum_{\beta=1}^{n}|c_\beta|^2 - 1\right) = 0,\ (1\le\alpha\le n), \quad \text{(A2a)}$$

$$\frac{\partial L_J}{\partial \lambda_\chi} = \sum_{\alpha=1}^{n}|c_\alpha|^2 - 1 = 0, \quad \text{(A2b)}$$

And

$$\frac{\partial L_J}{\partial \lambda_\kappa} = J_\kappa = 0,\ (1\le\kappa\le m,\ \kappa\neq\chi), \quad \text{(A2c)}$$

Respectively, where J_l(i.e.,$J_\chi$and J_κ) can be rewritten in terms of $\mathrm{Re}c_\alpha$ and $\mathrm{Im}c_\alpha$ as

$$J_l = \sum_{\alpha}^{n}\sum_{\beta}^{n}J_{l,\alpha\beta}\left(\mathrm{Im}c_\alpha\mathrm{Re}c_\beta - \mathrm{Re}c_\alpha\mathrm{Im}c_\beta\right)(1\le l\le m). \quad \text{(A3)}$$

By substituting the partial derivatives of J_l in **Eq. (A3)**, with respect to $\mathrm{Re}c_\alpha$ and $\mathrm{Im}c_\alpha$ into **Eq. (A2a)**, we obtain $2n+m$ coupled equations with $2n+m$ variables as

$$\sum_{\beta=1}^{n}J_{\chi,\beta\alpha}\mathrm{Im}c_\beta + \sum_{\kappa\neq\chi}^{m}\sum_{\beta=1}^{n}\lambda_\kappa J_{\kappa,\beta\alpha}\mathrm{Im}c_\beta + \lambda_\chi\mathrm{Re}c_\alpha = 0,\ (1\le\alpha\le n), \quad \text{(A4a)}$$

And

$$-\sum_{\beta=1}^{n}J_{\chi\beta\alpha}\mathrm{Re}c_\beta - \sum_{\kappa\neq\chi}^{m}\sum_{\beta=1}^{n}\lambda_\kappa J_{\kappa,\beta\alpha}\mathrm{Re}c_\beta + \lambda_\chi\mathrm{Im}c_\alpha = 0,\ (1\le\alpha\le n). \quad \text{(A4b)}$$

Equations (A2b), **(A2c)** can be expressed as

$$\sum_{\alpha=1}^{n}\left((\mathrm{Re}c_\alpha)^2 + (\mathrm{Im}c_\alpha)^2\right) - 1 = 0, \quad \text{(A4c)}$$

And

$$\sum_{\beta=1}^{n}\sum_{\alpha=1}^{n}J_{\kappa,\alpha\beta}\left(\mathrm{Im}c_\alpha\mathrm{Re}c_\beta - \mathrm{Re}c_\alpha\mathrm{Im}c_\beta\right) = 0\,. \quad \text{(A4d)}$$

Equation (A4) contains the final equations, which are the same as those in **Eq. 19**.

B BRIEF DERIVATION OF TARGET OPERATORS, CALCULATED USING THE COUPLED EQUATIONS FOR THE PERIMETER RING CURRENT (EQ. 20).

Similar to the ring current localization, the Lagrange functional for the perimeter ring current is given as

$$L_J^P(c_1,\cdots,c_n,\lambda_1,\cdots,\lambda_m) = J_P + \lambda_1 J_{B,1} + \cdots + \lambda_{m-1}J_{B,m-1} + \lambda_m\left(\sum_{\alpha=1}^{n}|c_\alpha|^2 - 1\right), \quad \text{(B1)}$$

Where J_P is the perimeter ring current (**Eq. 20a**) to be maximized, and $J_{B,l'}$ are the bridge bond currents (*see* **Eq. 20b**), which should be zero at the target time $t = T$, $J_{B,l'} = 0$ where $1\le l'\le m-1$. The last term indicates the normalization condition for the total target wave function $\sum_{\alpha=1}^{n}|c_\alpha|^2 - 1 = 0$.

In the same manner as the ring current is localized to a designated ring, the coupled equations for the perimeter ring current are obtained by taking partial derivatives of the Lagrange functional L_J^P (Eq. (B1)) with respect to $\mathrm{Re}c_\alpha$, $\mathrm{Im}c_\alpha$, and λ_l.

The coupled equations for the perimeter ring current can then be expressed as

$$\sum_{\beta=1}^{n}J_{\beta\alpha}^{P}\mathrm{Im}c_\beta + \sum_{l'=1}^{m-1}\sum_{\beta=1}^{n}\lambda_{l'}J_{\beta\alpha}^{B',l}\mathrm{Im}c_\beta + \lambda_m\mathrm{Re}c_\alpha = 0,\ (1\le\alpha\le n) \quad \text{(B2a)}$$

$$-\sum_{\beta=1}^{n}J_{\beta\alpha}^{P}\mathrm{Re}c_\beta - \sum_{l'=1}^{m-1}\sum_{\beta=1}^{n}\lambda_{l'}J_{\beta\alpha}^{B',l}\mathrm{Re}c_\beta + \lambda_m\mathrm{Im}c_\alpha = 0,\ (1\le\alpha\le n) \quad \text{(B2b)}$$

$$\sum_{\alpha,\beta=1}^{n}J_{\alpha\beta}^{B',l}\left(\mathrm{Im}c_\alpha\mathrm{Re}c_\beta - \mathrm{Re}c_\alpha\mathrm{Im}c_\beta\right) = 0,\ \left(1\le l'\le m-1\right) \quad \text{(B2c)}$$

And

$$\sum_{\alpha=1}^{n}\left((\mathrm{Re}c_\alpha)^2 + (\mathrm{Im}c_\alpha)^2\right) - 1 = 0. \quad \text{(B2d)}$$

C CALCULATED RESULTS OF TIME-DEPENDENT COEFFICIENTS $\{c_i(t)\}$ IN EQ. 31.

Equation 32 can be rewritten in the rotating approximation (RWA) as

$$\dot{c}_0(t) = -iV_{01}^a \exp(i\Delta_1 t)c_1(t) - iV_{02}^b \exp(i\Delta_2 t + i\zeta)c_2(t), \quad \text{(C1a)}$$

$$\dot{c}_1(t) = -iV_{01}^a \exp(-i\Delta_1 t)c_0(t), \quad \text{(C1b)}$$

$$\dot{c}_2(t) = -iV_{02}^b \exp(-i\Delta_2 t - i\zeta)c_0(t), \quad \text{(C1c)}$$

Where $\zeta \equiv \zeta_a - \zeta_b$ is the laser relative phase between the two lasers. Note that the laser phases ζ_a and ζ_b are transferred to the electronic states.

The coupled differential equations in Eq. (B1) are analytically solved under the two conditions described by **Eqs. 34a**, **34b** by setting the initial condition: $c_0(0) = 1$, $c_1(0) = c_2(0) = 0$ [43] such that

$$c_0(t) = \frac{\Delta^2 + V^2\left(e^{-i\Omega t} + e^{i\Omega t}\right)}{\Omega^2}, \quad \text{(C2a)}$$

$$c_1(t) = \frac{V}{2\Omega^2}\left[2\Delta e^{i\Delta t} + (\Omega - \Delta)e^{i(\Omega+\Delta)t} - (\Omega - \Delta)e^{-i(\Omega-\Delta)t}\right], \quad \text{(C2b)}$$

$$c_2(t) = -e^{-i\zeta}\frac{V}{2\Omega^2}\left[2\Delta e^{-i\Delta t} + (\Omega - \Delta)e^{-i(\Omega+\Delta)t} - (\Omega - \Delta)e^{i(\Omega-\Delta)t}\right]. \quad \text{(C2c)}$$